CHAPTER 4

Correlation Between Volcanic and Tectonic Segmentation of Fast-Spreading Ridges: Evidence from Volcanic Structures and Lava Flow Morphology on the East Pacific Rise at 9°-10°N

Abstract. Combined analysis of volcanic structures in DSL-120 sonar data and lava flow morphology in the *Argo* survey reveal consistent trends of effusion rate and volcanic structure within third-order tectonic segments, suggesting that third-order segmentation corresponds to volcanic segmentation. Along-axis changes in volcanic structures, from collapse troughs to lava domes, and lava morphology, from sheet to pillow flows, coincide with the third-order (volcanic) segmentation in the ridge crest visible in shipboard multibeam bathymetry. Pillow lava flows comprise 25% of the surveyed area of the ridge crest, found in close association with small lava domes 20 m high and 200 m across their base. An additional 25% of the surveyed area of the ridge crest is covered by sheet lava, found in close association with an axial collapse trough. The remaining terrain consists of lobate lava flows found throughout the area. Within the ~1 km wide axial zone, pillow lava domes, inferred to result from low effusion rate eruptions, occur primarily at third-order segment ends. In contrast, extensive collapses in lobate lava flows and lava channels lined with sheet lava, inferred to indicate much higher eruption effusion rates, characterize the axial zone away from the third-order segment ends. These observations suggest a tendency for eruption effusion rates to decrease at third-order segment ends consistent with a disrupted or inefficient volcanic plumbing system and demonstrate that third-order tectonic segmentation matches volcanic segmentation. Segmentation in the seismic structure of the axial magma chamber also correlates with morpho-structurally defined volcanic segmentation. Where a high sample density is available, erupted basalts are locally most fractionated near the ends of volcanic segments. We interpret the seismic, petrologic, and morpho-structural data as indicating that individual volcanic plumbing systems, organized at ~20 km spacing along the ridge axis (third-order segment scale), exist for each third-order segment. For fast-spreading ridges, we estimate that the longevity of volcanic segments is ~10^4-10^5 yrs, one to three orders of magnitude longer than fourth-order segments (~10^2-10^3 yrs). Therefore, the present pattern of hydrothermal activity may reorganize tens or hundreds of times while volcanic segmentation remains fairly stable.

1. Introduction

Understanding the causes of along-strike changes in eruptive processes provides important insights into the formation of new oceanic crust at fast-spreading ridges. In this study, we relate observations of volcanic structures and lava morphology from near-bottom acoustic and visual data to the structural segmentation of the East Pacific Rise (EPR) from 9°-10°N, and show how eruptive processes vary along the axis of this fast-spreading (~11 cm/yr full rate) ridge. Then, we combine the visual, sonar, petrological, and geophysical data to discuss the nature of volcanic systems on the EPR.

The concept of a volcanic system is useful in mid-ocean ridge volcanology, especially for the EPR where the term "volcano" may be misleading due to its common use as a synonym for volcanic edifice [*Simkin and Siebert*, 2000]. The system of fissures, dikes, and crater rows developed along-rift in association with a central volcano in Iceland is commonly referred to as a volcanic system [e.g.,*Gudmundsson*, 1995]. In this usage, a volcanic system refers to all of the features that share a common volcanic plumbing system. The process-oriented definition of volcanic system may be applied to the EPR, which does not ordinarily create a volcanic edifice at the ridge axis.

Volcanic segments would be defined by discontinuities in the volcanic system, or inter-volcano gaps. Previous work on the southern EPR, 17°-18.5°S, found that third order structural segmentation corresponds to volcanic segmentation, with each volcanic segment containing a single volcanic system [*White et al.*, 2000]. The third-order ridge axis offsets on the EPR, 15.5°-17°N, correspond to discontinuities in the seismic structure of the ridge crest also suggesting that volcanic systems are coupled to structural segmentation [*Carbotte et al.*, 2000]. We will show that the third order segmentation corresponds to volcanic segmentation on the EPR, 9°-10°N.

Axial discontinuities marking third-order segment boundaries are the finest order visible on multibeam bathymetry maps [*Macdonald et al.*, 1992; *Macdonald et al.*, 1988]. Several generations of regional bathymetry have been produced for the EPR between the 9°03'N OSC and Clipperton fracture zone [*Cochran et al.*, 1999; *Fornari et al.*, 2000; *Macdonald et al.*, 1992; *Wilcock et al.*, 1993]. For most of the study area, we used a 100 meter grid of *Cochran et al.* [1999] to identify third-order segments. This grid does not extend the full length of our study area, so we combined the bathymetry from *Cochran et al.* [1999] and *Macdonald et al.* [1992] to pick the remainder of the segments in the study area.

All of the third-order segment boundaries were picked solely from the multibeam bathymetry (Figure 1). Subsequently, the DSL-120 sonar records collected in March 2000 were used to refine these picks to 185 m (0.1') precision (Table 1). The third-order segmentation is defined by a resolvable (>200 m) offset to the continuous linear axial trace, or a significant (>20 m) local bathymetric saddle in the smooth convex-upward bathymetric profile. This definition differs slightly from that proposed by *Macdonald et al.* [1992] as explained by *White et al.* [2000]. Fissure swarms, the axial summit collapse trough (ASCT), and smaller collapse pits visible on the DSL-120 records establish a continuous axial trace that we were able to follow into fine-scale overlap zones that are below the resolution of the multibeam bathymetry maps. Note that re-picking the segment ends from DSL-120 records improves only the precision of the initial picks from multibeam bathymetry, not their accuracy.

EPR morphology from 9°-10°N is typical of fast-spreading ridges [*Carbotte and Macdonald*, 1994]. Multibeam bathymetry reveals that the first-order ridge segment between the Clipperton and Siquieros transform faults is offset by the 9°N OSC, a second-order offset [*Macdonald et al.*, 1992]. Within the second-order segment from the OSC at 9°N to the Clipperton transform, the ridge axis maintains a minimum depth in the range of 2500-2600 m. The general cross-sectional shape of the axial region changes abruptly from a narrow, triangular ridge crest at the ridge intersection with the Clipperton to a broad rectangular axial high, maintains this rectangular cross-sectional shape for half the segment, then gradually tapers southward to a domal and then a triangular shape approaching the 9°N OSC [*Macdonald and Fox*, 1988]. The calculated cross-sectional area of the axial high exhibits the same pattern of abrupt increase in axial cross-section south of the Clipperton and subsequent gradual decrease southward to the 9°N OSC [*Scheirer and Macdonald*, 1993]. Two significant local minima in the cross-sectional area are particularly apparent at 9°57’N and 9°21’N which correspond to two third-order segment boundaries [*Scheirer and Macdonald*, 1993].

In addition to multibeam bathymetry, 9°-10°N EPR is the site of many other studies critical to understanding the nature of the volcanic systems along fast-spreading ridges. The *Argo* photoacoustic sled was used to survey the ridge crest from 9°09'-54’N in 1989 [*Haymon et al.*, 1991]. The 1989 *Argo* survey provides detailed lava morphology observations used here, and information on hydrothermal distribution, tectonic features and very-high resolution 100 kHz sonar images from previous work [*Fornari et al.*, 1998; *Haymon et al.*, 1991; *Wright et al.*, 1995a]. The DSL-120 side-scan sonar system was used to survey the ridge crest from 9°08'-10°02’N in March 2000. We use the DSL-120 data to

examine the meso-scale ridge crest structures such as: axial lava mounds, ASCT segments, fissure swarms, and lava distribution systems (tubes and channels). Numerous rock sample analyses indicate variability in the magmatic system within the second-order segment [*Batiza and Niu*, 1992; *Langmuir et al.*, 1986; *Perfit et al.*, 1994; *Smith et al.*, 2001]. Several studies of the seismic structure of the axial region provide a means for correlating our observations of volcanic structures to characteristics of the magmatic system [*Detrick et al.*, 1987; *Dunn et al.*, 2000; *Harding et al.*, 1993; *Kent et al.*, 1993a; *Kent et al.*, 1993b; *Toomey et al.*, 1994; *Vera and Diebold*, 1994].

2. Volcanic Structures Imaged by DSL-120 Sonar

2.1. Data Acquisition

Volcanic structures formed on the ridge crest of the EPR are commonly tens to hundreds of meters long , inconveniently falling between the optimum resolution of sea-surface sonar systems (~100 m pixel resolution), and mixed optical-acoustic observations from occupied submersibles and remotely operated vehicles (~20 m total swath width). Prior to 2000, side-scan sonar data of the study area consisted of SeaMARC II coverage of the ridge axis [*Macdonald et al.*, 1984], a short SeaMARC I swath between the Clipperton and 9°54’N [*Kastens et al.*, 1986], and several ~300 m wide swaths of *Argo* 100 kHz sonar from 9°54’N to 9°08’N [*Fornari et al.*, 1998]. In 2000, DSL-120 side-scan sonar and phase-bathymetry data were obtained continuously along the ridge axis from 9°08'-10°N (Figure 1). The DSL-120 sonar survey provides complete coverage at the intermediate scale needed to clearly resolve the volcanic structures on the EPR crest.

The DSL-120 sonar operates at 120 kHz, and has an effective near-nadir pixel resolution of 1 m for side-scan backscatter imagery and 4 m for phase bathymetry, when towed at ~1 knot at ~100 m altitude [*Scheirer et al.*, 2000]. Under these conditions, we obtained a 900-1000 m wide backscatter reflectivity swath and a 700-800 m wide bathymetry swath. Two overlapping parallel lines were run from 10°02’N to 9°36’N, and one line was continued south to 9°08’N. A perpendicular crossing line was run at 9°37’N. Neither the crossing line nor the overlapping areas showed any systematic bias in the bathymetry values after processing. The side scan backscatter reflectivity measures the amplitude of the acoustic return, which appears to be primarily influenced by the slope and roughness of seafloor in axial zones for 120 kHz sound [*Scheirer et al.*, 2000; *Stewart et al.*, 1994]. Bottom-moored transponder navigation was available from 9°34’N to 9°38’N. Navigation for the rest of the survey was determined by a layback-correction for the DSL-120 towfish position calculated from ship speed

and the length of wire paid out relative to P-code GPS defined ship position. Comparison of distinctive features in overlapping DSL-120 swath indicates that the layback navigation was self-consistent to within ~100 m. Prior work with the bottom-moored transponders indicates that they are accurate to within 5-10 m in global geodetic navigational coordinates [*Fornari et al.*, 1998].

2.2. Observations of Volcanic Structures

Lava mounds and the collapse troughs are the two most well-defined volcanic structures in DSL-120 sonar data (Figure 2). In addition, we interpret several low-reflectivity areas in the DSL-120 backscatter imagery and long sinuous collapses in the DSL-120 backscatter and bathymetry as lava distribution systems (channels or collapsed tubes), based on their morphology, proximity to areas of known lava channels [*Fornari et al.*, 1998; *Haymon et al.*, 1991], and general association with sheet lava flows. Axial lava mounds, collapse troughs, and lava distribution systems are the same volcanic structures that were identified in the 1996 DSL-120 survey on the southern EPR [*White et al.*, 2000].

Dominating the axial zone from 9°52'N to 9°23'N, the ASCT appears as a series of long depressions in the DSL-120 bathymetry, and as paired weak-strong backscatter reflections with the weaker reflection nearest to the sonar towfish (Figure 2). In our study area, the ASCT may be divided into three distinct collapse structures which correspond to three third-order segments. A narrow ASCT segment, ~50m wide and ~10-20m deep from 9°45'N to 9°52'N, is separated across a zone of small-scale collapse and fissuring from a wider ASCT segment, ~400m wide and ~20m deep from 9°43.5'N to 9°36.4'N. A similar wide ASCT segment begins at a right-step overlapping offset at 9°37.1'N and continues to 9°23'N (Table 1). Lava distribution systems emanating from the ASCT indicate high effusion rate eruptions and transport of lava at least a few hundred meters down the ridge flanks. Previous studies have provided detailed descriptions of the ASCT in our study area [*Fornari et al.*, 1998; *Haymon et al.*, 1991].

Lava mounds appear as quasi-circular paired reflections indicating a mound-shaped structure, and show up as topographic highs in the side-scan phase-bathymetry (Figure 3). Their shape is generally a smooth convex-upward hemispherical dome that rarely shows evidence of summit collapse. The nature of the DSL-120 sonar return from the lava mounds limits the size of the features we observe to those that are large enough have a consistently recognizable mound shape (~20 m base radius) but not so large that their perimeter falls outside the side-scan swath (~500 m base radius). However, lava mounds wider than the DSL-120 swath would be resolved on multibeam bathymetry if

such mounds existed. A few small pillow constructions (haystacks) are known to exist from near-bottom visual observations but are not included in the same category as the larger lava mounds for several reasons, as follows. Haystacks are difficult to identify on DSL-120 records without ground-truth from visual observations. Also, edifices of this small size may be imaged incompletely, especially in the phase-bathymetry, and are difficult to measure accurately. Haystacks and larger lava mounds could result from similar eruptive processes, but haystacks would be volumetrically insignificant in comparison to the lava mounds.

The average radius of the lava mounds in our study area is 125 m, and their average height is 20 m, within one standard deviation of the mean from their counterparts on the southern EPR which have an average radius of 100 m and average height of 20 m. In comparison to the EPR axial lava mounds, the small seamounts on the Mid-Atlantic Ridge are typically larger (~60 m characteristic height) and exhibit a greater range in size [*Smith and Cann*, 1999; *Smith et al.*, 1995]. Pillow mounds found on the Juan de Fuca Ridge and the EPR are similar in size [*Embley and Chadwick*, 1994; *Embley et al.*, 2000].

2.3. Definition of the Axial Zone

The axial zone refers to a 1 km wide corridor centered on the ridge axis where all of the geological features are representative of the present volcanic processes occurring at the ridge, and exclude as many of the older, relict features as possible. The 1 km width was chosen to most closely match the width of the axial zone in this study with other studies of active volcanic processes in this area [*Haymon et al.*, 1993; *Haymon et al.*, 1991; *Kurras et al.*, 2000; *Perfit et al.*, 1994; *Smith et al.*, 2001] and on the southern EPR [*White et al.*, 2000]. Additionally, we found lava mounds beyond ~500m from the ridge axis that appear to be dissected by faults (Figure 4). Faulting suggests that these may be old, inactive structures in the process of being destroyed, and are not representative of current volcanic processes on-axis.

The volcanic structures of interest in this study are those created by the axial eruptions of the current volcanic systems on the EPR, in other words, those occurring within the axial zone. Beyond this zone, flow fronts of lava flows originating at the axis are a potential source of pillow lava that may be interspersed with off-axis volcanic constructions [*Kurras et al.*, 2000; *Perfit et al.*, 1994]. Volcanic structures may be destroyed by the initiation of normal faulting within a few hundred meters of the ridge axis [*Carbotte and Macdonald*, 1994; *Fornari et al.*, 1998]. All of these factors obscure the

pattern of volcanic structures and lava morphology generated by axial eruptive processes. For this reason, we limit our study to within 500 m of the ridge axis where we can be reasonably sure there is an accurate record of recent eruptive processes.

2.4. Recognition of Axial Pillow Lava Domes

We infer that the lava mounds formed within the axial zone may be classified as lava domes. Lava domes differ from lava mounds in that domes have a specific genetic definition, while mounds are any mound-shaped feature. Lava domes are a steep-sided pile of lava formed by eruption of short lava flows or intrusion into the lava pile over the primary volcanic vent [*Williams*, 1932].

The lava domes within our study area meet the same criteria used by *White et al.* [2000] to identify pillow lava domes on the southern EPR. The lava domes in our study area are dominantly composed of pillow lava, and are morphologically similar to lava domes in the axial zone on the southern EPR (Figure 5). Areas with lava domes are areas where pillow lava is commonly observed from *Argo*, *Alvin*, or WHOI camera tow images [*Engles et al.*, 2000; *Haymon et al.*, 1991; *Smith et al.*, 2001]. Pillow lava flows spread slowly, causing lava to pile up around its eruptive vent thus forming lava domes [*Gregg and Fink*, 1995; *Griffiths and Fink*, 1992]. The ridge crest within our study area has a regional along-strike gradient of ~1 m/km making it highly unlikely that lava could be transported along-strike by gravitationally driven flow through lava tubes and form ~20 m high mounds. Further, the lava domes appear to be independent lava flow units from observations of sediment cover and cross-cutting relationships, rather than part of one long lava flow as expected for secondary volcanic edifices. The classification of lava domes may only apply to those lava mounds found within the 1 km wide axial zone, because slope gradient may be considerably higher on the ridge flanks.

2.5. Volcanic Structures and Third-Order Segments

The third-order segment boundaries identified in multibeam bathymetry correspond to the areas of pillow lava domes and to breaks in the continuity of the ASCT. It is significant that both of the gaps between ASCT segments, the fissure-cut relay zone from 9°43.5’N to 9°45’N and the overlapping ASCT segments around 9°37’N, are third-order segment boundaries in the multibeam bathymetry. Where the ASCT is continuous, no segment boundaries are found.

Pillow lava domes are associated with 4 out of 5 third-order segment boundaries identified from multibeam bathymetry (Figure 6). When lava domes within only 250 m of the axis are considered instead of those within the full width of the axial zone, a smaller total number of lava domes are still associated with 4 of 5 segment ends. This implies that our result is not uniquely produced by the particular width defined for the axial zone.

The absence of any lava domes at the third-order segment boundary at 9°45'N merits further comment. This offset of the ridge axis is apparent in multibeam bathymetry, and is a prominent structural discontinuity in the ASCT in the DSL-120 records as well (Figure 7). The axial zone exhibits a swarm of fissures in older terrain at the southern edge of an area that experienced an eruption in 1991 [*Haymon et al.*, 1993]. Although no lava domes occur, pillow lavas are found in abundance, and may be forming small pillow haystacks. The third-order segment boundary at 9°44.8'N is less distinct than any of the others in this study. Perhaps it is just developing, or is being overprinted. As *Macdonald et al.* [1988] point out, segmentation of oceanic ridges is a continuum, and not all segment boundaries will fit easily into one classification.

The absence of lava domes at 9°45'N highlights an interesting difference between volcanic structures on the EPR at 9°-10°N and those at 17°-18.5°S. Pillow lava domes are rare at 9°-10°N, and located exclusively at segment ends; whereas lava domes at 17°-18.5°S are found all along the ridge but occur much more abundantly at segment ends. In contrast, the collapse troughs forming the ASCT are quite extensive at 9°-10°N, covering most of the length of three third-order segments, whereas the collapse troughs at 17°-18.5°S are much smaller and cover only ~25% of the total third-order segment length of two segments out of eight. However, all of these ASCT structures probably result from extensive lava carapace collapse [*Fornari et al.*, 1998]. While it is clear that the eruption history of the EPR at 9°-10°N is different from that at 17°-18.5°S, the overall distribution of volcanic structures with respect to third-order segmentation is similar.

3. Lava Flow Morphology

3.1. Data Acquisition and Analysis

Visual observations of lava flow morphology in the axial zone of the EPR from 9°09' to 9°55'N were obtained in November 1989 using multiple camera systems on *Argo* [*Haymon et al.*, 1991]. The axial zone was surveyed in long, axis-parallel lines from 9°08' to 9°54'N. *Argo* was towed 7-10 m above the bottom, resulting in a 10-16 m visual swath width [*Wright et al.*, 1995a]. For this

study, we use several long, axis-parallel *Argo* tracklines spaced 10-50 m apart. This set of track lines provides dense visual coverage within the ASCT but the coverage density decreases with distance from the ridge axis (Table 2). *Haymon et al.* [1991] describe the *Argo* survey logistics in detail. Lava flow morphology data was tabulated during the 1989 survey, but not quantitatively analyzed until now.

We have compiled the real-time lava morphology data from the 1989 *Argo* survey, reclassifying the detailed original observations into three categories: sheet, lobate, and pillow lava flows. Sheet lava flows are all of the smooth, ropy, or hackly lava flows logged during the *Argo* survey. Lobate lava flows remain unchanged from the real-time *Argo* classification scheme. Pillow lava flows include both bulbous and tubular pillows logged during the *Argo* survey. Examples illustrating the variations in appearance used to classify lava morphology from this area are presented in *Kurras et al.* [2000]. Lava morphology observations logged in real-time were spot-checked against photographs taken at the same time during the *Argo* survey to ensure that the logged observations were accurate records of the lava morphology. For another check of the accuracy of the real-time observations, the lava morphology at points where the *Argo* lines crossed was checked in the geographic information system database to see if both observations were the same. We found that in most cases, the observations were in agreement suggesting a high level of internal consistency in the data. The reclassified sheet, lobate, and pillow categories correspond to high, medium, and low lava effusion rates, respectively [*Gregg and Fink*, 1995].

To construct the maps of lava morphology, we applied the conversion of point observations to areas used by *White et al.* [2000] for *Argo* II data on the southern EPR by modifying the procedure described by *Wright et al.* [1995a] for mapping lava age distributions. The *Argo* observations were made at random intervals, usually after crossing a lava morphology contact, and logged at a specific time. Thus, the lava morphology observation data consist of points in space defined by the position of *Argo* when the observations were made. Because these points actually represent areas, the number of observations of a given lava morphology has no intrinsic meaning, and must be adjusted by the area that the observation represents. To do this, all of the original point observations are expanded into areas where the size of the area corresponds to the spacing between the data points by the point-in-polygon method. This point-to-area conversion works well for statistical comparisons of regions, but it can result in some repositioning of contacts, thus making it unsuitable for making geologic maps of specific areas. To compare the variability of lava morphology to third-order segmentation, we require

a statistical quantification of lava morphology within ~20 km long segments rather than a precise map of an area, so this method is adequate for our purposes.

To determine the variation in lava morphology within the third-order segments, we bin the data by latitude along the axial zone to examine the variation displayed over each volcanic system independently. Because the volcanic systems are 15-30 km long, we chose a 2' (~4 km) bin interval as the optimal length to have enough bins to emphasize regional trends, while minimizing noise in the data.

3.2. Observations

The low-effusion rate pillow flows and high-effusion rate sheet flows are anti-correlated by latitude, an initial indication that the distribution of lava morphology has a large-scale organization. By latitude, pillow and sheet lava flow morphology show more variation in relative abundance overall than lobate lava flows (Figure 8). The relative abundance of pillow compared to sheet lava flows is closely related to the third-order segments. Pillow flows are limited to ends of the ASCT segments, and are otherwise completely absent within the ASCT. In contrast, the abundance of lobate lava flows varies surprisingly little in the study area.

The pillow lava abundance reaches local maxima near each of the third-order segment ends (Figure 8). Abundant pillow lava corresponds to pillow lava domes in most locations. However, the 9°44.8’N third-order segment boundary has a prominent local maxima in pillow abundance that is unrelated to formation of pillow lava domes. In this instance, the distribution of lava morphology indicates the trend toward decreased lava effusion rate in the absence of recognizable pillow lava domes.

Observations by latitude may be affected by the locations of the *Argo* tracklines. For example, the segment boundary at 9°36'-38’N was surveyed by towing *Argo* up one ASCT limb, then angling across the overlap zone to the next ASCT, so that the segment ends were missed (Figure 2). As a result, this area appears to have a lower percentage of pillow lava than it would show if coverage was extended to the segment ends [*Engles et al.*, 2000; *Smith et al.*, 2001]. Even so, this area still shows a small local increase in the abundance of pillow lava relative to the surrounding areas (Figure 8). Checking the *Argo* tracks against the DSL-120 records, we believe that *Argo* coverage was sufficiently extensive that a representative sampling of lava morphology was obtained.

Overall patterns in lava morphology in our study area exhibit some differences from the distribution noted in earlier work on fast-spreading ridges that relied on more limited camera-tow or submersible observations [*Auzende et al.*, 1996; *Gente et al.*, 1986; *Kurras et al.*, 2000; *McConachy et al.*, 1986; *Renard et al.*, 1985]. Out of the total area visually imaged by *Argo*, approximately 25% is pillow lava, 50% is lobate lava, and 25% is sheet lava. Fast-spreading ridges had been thought to erupt primarily (~80-90%) sheet flows in the neovolcanic zone [*Bonatti and Harrison*, 1988; *Perfit and Chadwick*, 1998]. This is not the case although sheet and lobate flows together do cover most of the axial zone. Pillow flows are nearly twice as abundant as previously estimated.

Sheet flows show an abundance pattern related to the ASCT in addition to a correlation with the centers of third-order segments. Sheet flows are more abundant in the third-order segments where an ASCT is present. Sheet flows generally cover 25-50% of the total area imaged by *Argo* in and surrounding the ASCT between 9°23' and 9º52’N (Figure 8). Otherwise, sheet flows generally cover less than 10% of the total area imaged by *Argo* in areas without an ASCT. This is similar to the lava morphology distribution on the southern EPR, where sheet lava flows were sparse (< 10% of total imaged seafloor) except in the region surrounding Aldo Lake trough [*White et al.*, 2000].

4. Relationship Between Volcanic Effusion Rate and Volcanic Structure in Axial Zone

To quantify the relationship of third-order segmentation to volcanic segmentation for all of the segments in the study area, the number of lava domes and the relative abundance of each lava morphology, respectively, are stacked to obtain a cumulative distribution with respect to location within the third-order segments. Individual volcanic segments are likely to be in different stages of volcanic activity at any particular time. For example, even though pillow lava domes tend to occur near segment ends most of the time, any given segment at any particular time might have a sheet flow covering significant parts of the segment end [e.g., *Engles et al.*, 2000]. In order to reduce the effects of temporal variation, we stack all four complete third-order segments in our study area together.

To account for segments of different lengths, we used a percentage distance calculated from the centroid of each lava dome base to the segment end, divided by half the total segment length. The same procedure was used for lava morphology, except that the area of each lava morphology had to be divided into discrete blocks of arbitrary size, based on a subdivision of the point-to-area conversion, so that the distance of each block from the segment end can be measured. This calculation gives the percent distance from the segment end as a method of normalizing for segments of different lengths.

The data were divided into five bins along-axis, each representing 20% of the total segment length. The five bins are enough data points to define a trend while minimizing errors due to small numbers of observations or unequal survey coverage.

Once normalized to segment length, both the abundance and total base area of lava domes decrease dramatically from segment end to segment center (Figure 9a). In fact, over half the total area covered by lava domes lies within the 20% of the area closest to a segment end, and no lava domes are found in the middle 40% of the segments. Note that this calculation only uses the four segments where we have complete DSL-120 coverage; in addition, ten more lava domes are actually observed in the DSL-120 data near third-order segment ends that are not included in Figure 9a.

When the lava morphology data from all four complete segments in the study area are stacked and normalized to segment length, the relative abundance of pillow lava flows decreases with distance away from third-order segment ends (Figure 9b). Sheet lava flows show the opposite relationship: an increase with distance away from third-order segment ends (Figure 9b). The abundance of lobate lava flows shows very little variation within third-order segments, indicating that local eruption processes are dominated by conditions that will produce lobate lava flows.

The lava morphology data along third-order segments indicate systematic trends in the kilometer-scale distribution of lava flows, instead of a random distribution. Variations in the lava effusion rate, slope of the pre-existing seafloor, or lava viscosity may be causing random changes in lava morphology on small scale (<100 m), but this random meter-scale variability in individual lava flows occurs within a more organized overall distribution of lava morphology revealed by along-strike *Argo* mapping over several kilometers. The anti-correlation of pillow and sheet lava flows (Figure 9) acts as the critical discriminant in the study area, and suggests that eruptions at one location tend to produce either high or low effusion rate lava flows over time.

The effusion rate of eruptions appears to play an important role in the development of volcanic structures on the ridge axis. High effusion rate eruptions are the most likely to create thin-crusted lava ponds with numerous lava pillars and flat lobate and sheet flows [*Gregg and Chadwick*, 1996]. Our observations of lava morphology show that sheet flows are most common around the ASCT, corroborating the suggestion that high effusion rate eruptions result in ASCT formation [*Fornari et al.*, 1998; *Haymon et al.*, 1991] (Figure 8). In contrast, lava domes are formed when lava piles up around its eruptive vent, and indicate lower effusion rate eruptions. Our observations of lava

morphology show that, overall, pillow lava flows are most abundant in the places where the axial pillow lava domes form. The tendency for pillow domes to form near third-order segment ends suggests effusion rates correspondingly decrease within third-order segment boundary zones.

What if the axial pillow lava domes were actually secondary (rootless) volcanic edifices and not true lava domes at all? Although we have good circumstantial evidence that the small pillow lava domes exist in the axial zone, the possibility still exists that some of these domes are really secondary volcanic edifices. Even if true, this difference would not affect our interpretation of organization of volcanic systems along the ridge. In fact, it would imply that most eruptions occur near the middles of segments, which requires an even more focused magma supply than our preferred interpretation of the pillow mounds as lava domes forming within the axial zone.

5. Correlative Evidence for Volcanic Segmentation

The observed variation in volcanic structure and lava morphology within third-order segments suggests disrupted or inefficient magma delivery to the eruptive vents near segment ends that is characteristic of volcanic segmentation. The segmentation of volcanic systems may also be manifested in the chemistry of the lava, the structure of the crust, and the geometry of magma reservoirs. The results of numerous studies of crustal structure and composition on the EPR at 9°-10°N show some correlation with volcanic segmentation as detailed in this section.

5.1. Seismic Imaging of the Axial Magma Chamber

Seismic reflection profiles at 9°-10°N show prominent axial magma chamber (AMC) reflectors ~1500 m below the seafloor under most of the ridge axis [*Detrick et al.*, 1987]. Eight seismic profiles perpendicular to the ridge and a 3-D tomographic study provide additional constraint on sub-surface structure [*Kent et al.*, 1993a; *Kent et al.*, 1993b; *Toomey et al.*, 1994]. Spatial correlation between segmentation of the AMC and third-order segmentation would provide evidence that third-order segments are separate volcanic systems [*Sinton and Detrick*, 1992]. Gaps between volcanic systems may correspond to changes in the depth and width of the AMC imaged in seismic reflection profiles. However, large changes in the melt:crystal ratio in the AMC are found even where the AMC is apparently continuous along-strike [*Singh et al.*, 1998]. Thus, the segmentation of the AMC to along-axis magmatic flow may be indicated by subtle changes in its seismic characteristics.

Each of the third-order segment boundaries correspond to some type of discontinuity in the AMC (Table 1). A break in the AMC reflector is noted in the 9°57'N third-order segment boundary zone [*Detrick et al.*, 1987; *Vera and Diebold*, 1994]. The depth to the AMC increases and the width decreases by ~200 m at 9°45'N compared to the next closest seismic profile to the south across the ridge [*Kent et al.*, 1993a]. Seismic imaging indicates a pinch-out of the AMC occurs at the segment boundary centered on 9°37'N [*Kent et al.*, 1993a; *Toomey et al.*, 1994]. *Kent et al.* [1993a] infer a right-lateral jump of the AMC associated with an increase in AMC width at the 9°20'N segment boundary. Another break in the AMC reflector was found in the 9°10'-12'N third-order segment boundary zone [*Detrick et al.*, 1987; *Kent et al.*, 1993b]. Only one seismic discontinuity has been proposed that fails to correspond to the third-order segment discontinuities, an anomalous high seismic velocity at 9°28'N near the depth of the AMC [*Dunn et al.*, 2000; *Toomey et al.*, 1994]. The nature of this discontinuity is equivocal, because it is only seen in the seismic tomography data as a small velocity increase near the edge of the tomographic survey box and is not apparent where at the depths where the AMC should be present [*Dunn et al.*, 2000; *Toomey et al.*, 1994]. Further, no discontinuity appears at 9°28'N in the seismic reflection profile of the AMC [*Detrick et al.*, 1987; *Kent et al.*, 1993a] or in seafloor morphology (this study and *Haymon et al.*[1991]). Otherwise, third-order ridge discontinuities identified from the ridge morphology match the locations of disruptions to the AMC indicated by seismic studies.

5.2. Geochemical Variations

The geochemical composition of axial basalt has been shown to correlate with ridge crest segmentation which can be related in turn to the organization of magmatic plumbing systems. Initial results from along-axis dredging (>5 km spacing) between 9°17'N and 9°51'N suggested geochemical discontinuities consistent with devals located at 9°20'N, and 9°53'N [*Langmuir et al.*, 1986]. Additional sampling at ~2 km spacing produced results consistent with either a single, narrow, chemically zoned magma chamber beneath the ridge in this region, or a single geochemical discontinuity at 9°37'N [*Batiza and Niu*, 1992]. However, volcanic segment (third-order) discontinuity zones that we have identified span only ~3 km along-axis, so sample spacing on a finer scale than this is necessary to resolve the segmentation. Dense sampling (10-500 m spacing) in the axial zone from 9°28'N to 9°56'N using *Alvin* [*Perfit and Chadwick*, 1998; *Perfit et al.*, 1994; *Smith et al.*, 2001] provides an adequate sample spacing to resolve the volcanic segment discontinuity zones.

Geochemical discontinuities are typically expressed as significant changes in lava composition, differences incompatible element ratios or isotopes, or great variability in lava chemistry [e.g.,*Batiza and Niu*, 1992; *Langmuir et al.*, 1986; *Perfit et al.*, 1994; *Smith et al.*, 2001]. Distinct differences in trace element or isotopic characteristics would be consistent with separate mantle sources and magma plumbing systems. Extremely variable lava composition with similar source characteristics may indicate an inefficient volcanic plumbing system or restricted magma reservoirs such as might exist at the ends of a volcanic segment. Such variability might be less surprising in light of the complex geology we observe in the volcanic segment boundary zones where pillow lava domes and lobate flows may interfinger or even be overprinted by the occasional lava channel. However, it illustrates why multiple well-located samples are needed to establish the range of variability of lava compositions at volcanic segment boundaries. Rock samples collected from Alvin dives provide the type of closely-spaced well-located samples necessary to discern the geochemical signature on the scale of third-order segments. For example, *Smith et al*. [2001] document a geochemical discontinuity in lava composition and hydrothermal fluid chemistry associated with the ~500 m wide 9°37’N discontinuity. The range of axial basalt compositions within the bounds of the 9°37’N discontinuity zone is strikingly large, being nearly as great as it is along the entire second-order segment from 9°03’N to 10°N. *Smith et al.* [2001] also suggest the eruption of E-MORB and evolved N-MORB at the dying limb of the OSC are a consequence of it marking the end of volcanic segment.

The extensive suite of samples from 9°30'-56’N allows us to examine the geochemistry across three third-order segment boundaries. For the purposes of this study, we restrict our comparison to Mg# ($Mg/Mg+Fe^{2+}$) [*Perfit et al.*, 1994; *Smith et al.*, 2001]. The Mg# generally indicates how evolved a particular lava is, and can be used as a proxy for magma temperature. Lava with an Mg# in the 65-70 range is considered relatively primitive whereas lower numbers reflect an increasing extent of fractional crystallization and cooler magma temperatures. Crystal fractionation is enhanced in smaller, cooler, or more poorly mixed magma reservoirs such as those expected at volcanic segment boundaries. Decrease in Mg# with decreasing latitude south of 9°50’N was previously ascribed to decreasing temperatures due to thermal and chemical zonation of single central magma source [*Batiza and Niu*, 1992]. However, the range of Mg# at the 9°37’N discontinuity nearly encompasses the entire range along axis.

Because we are looking for what may be small disruptions in the magmatic system, the minimum Mg# sample is used to indicate where the most fractionated lava erupts (Figure 10). Within each of the two well-sampled segments, the samples with lowest Mg# are found closest to the segment ends. Also, the samples with the highest minimum Mg# are found at the centers of the third-order segments, although the samples with maximum Mg# values do not necessarily occur there (Figure 10). Where we have good sample density, we conclude that the most fractionated lava does correspond with third-order segment ends. Further work in this area is needed to establish the relationship between the lava geochemistry and third-order segmentation.

5.3. Fissure Width

The distribution of fissures at the seafloor indicates the scale and extent of mechanical failure of the upper crust that may have implications for the size and distribution of volcanic vents, as well [*Wright et al.*, 1995a]. Based on a theoretical relationship of width to depth for tensile (mode I) fissures, *Wright et al.* [1995b] suggest that wide fissures may penetrate the layer 2A/2B transition and serve as eruptive conduits. Only some of the widest fissures are likely to be eruptive fissures. Further, eruptions forming pillow lava over the eruptive vent are unlikely to leave visible fissures due to minimal lava drainback after the eruption. Also, the final width of the fissure may be highly modified by lava drainback or mass wasting. In spite of these uncertainties, the interpretation of *Wright et al.* [1995b] that the eruptive fissures are the widest fissures is probably accurate where lobate flows are the dominant lava morphology.

The majority of the widest fissures (>4 m), most likely to be eruptive fissures, are found outside the third-order segment boundary zones (Figure 11). These fissure width data, collected with *Argo* in 1989 [*Wright et al.*, 1995b], were binned in 3.7 km (2') intervals to compare with the other data at this bin interval. Generally the average fissure width in each bin is lower near the segment ends, although south of 9°35’N are many fissures <1 m wide that may not be eruptive fissures (Figure 11). One local exception to the trend is at 9°14'-18’N where glassy, unsedimented lava flows were found. Since this data was collected prior to the 1991 eruption [*Haymon et al.*, 1993], the fissure data north of 9°45’N are not affected by that event.

If the width of dikes that feed eruptions is proportional to the width of eruptive fissure, then our observations imply that eruptive dikes are generally narrower at segment ends than at segment centers. The maximum width of the *Argo* fissures is ~8 m and the average varies from 1 to 3 m in each

bin in Figure 11. The average width for surface fissures is only slightly greater than the widest dikes typically found in oceanic crust [*Karson*, 1998; *Karson et al.*, 1992]. Given the many factors that could cause the fissure width to differ from the eruptive dike width, we can only speculate that the eruptive dikes may be proportional in width to the eruptive fissures.

6. Discussion

6.1. Volcanic Segmentation: How does it differ from Fourth-order segmentation?

The correlation of morpho-structural, seismic, and geochemical discontinuities indicates that third-order segmentation of volcanic systems affects the entire crustal section. In contrast, fourth-order segments originally were defined as morphologically distinct segments created by eruptive fissures that probably changed with each new eruptive episode [*Haymon et al.*, 1991; *Macdonald et al.*, 1988]. On the basis of much finer-scale seafloor mapping, *Haymon* [1996] predicted that the hydrothermal systems are controlled at the fourth-order scale by individual dike injections or eruptions. These predictions were largely corroborated by time-series studies of the hydrothermal vents on the NEPR that found compositional changes in the hydrothermal vent fluid were influenced by a single eruption [*Von Damm*, 2000; *Von Damm et al.*, 1995]. Hydrothermal systems are also sensitive to the structure of the volcanic carapace such that the widest fissures, especially those associated with the ASCT, tend to become preferential conduits for hydrothermal flow [*Wright et al.*, 1995a].

Each new episode of dike injection and eruption on the EPR has the potential to reorganize hydrothermal circulation by changing the thermal properties and permeability of the upper crust within existing third-order segments. Dike injection appears to be centralized at one location on some third-order segments (e.g. 9°10.4'-21'N / fourth-order segment G) or distributed into several segments on others (e.g. 9°19'-37.9'N/ fourth-order segments D, E, and F) (Figure 1). Some volcanic segments may change their position or geometry over time by propagating along axis leaving faint migration traces [*Cormier et al.*, 1996; *Lee et al.*, 1996; *Smith et al.*, 2001]. Otherwise, we infer that only large magmatic events would cut through and reorganize volcanic segments. In either case, estimates for the longevity of volcanic segments (~10^4-10^5 yrs) are one to three orders of magnitude higher than for fourth-order segments (~10^2-10^3 yrs) [*Macdonald et al.*, 1992; *White et al.*, 2000]. Therefore, the present pattern of hydrothermal segmentation may reorganize tens or hundreds of times while volcanic segmentation remains fairly stable.

2.2. Cause of the Lava Flow Morphology Variation Within Volcanic Segments

The EPR exhibits an unusual pattern in the variation of volcanic effusion rate compared to other volcanoes. Evidence suggests that the lowest effusion rate eruptions tend to occur at the distal ends of the volcanic segments. Typically on basaltic rift volcanoes, higher effusion rate eruptions are observed on the distal flanks of the volcano [*Basaltic Volcanism Study Project*, 1981]. For example, extensive lava flows at the distal end of the East Rift of Kilauea Volcano are thought to be more voluminous and have higher effusion rates than summit eruptions [*Holcomb*, 1987; *Holcomb et al.*, 1988; *Lonsdale*, 1989]. Also, *Sigurdsson and Sparks* [1978] suggest that the most extensive lava flows in Iceland, corresponding to highest effusion rates, result from draining the summit reservoirs of central volcanoes into the volcanic rift zones. The fundamental cause for higher effusion rates in lower, more distal eruptions is that the volume and peak effusion rate of eruptions tends to decrease as the elevation of the eruptive vent increases [*Epp et al.*, 1983]. The magma pressure needed to drive an eruption increases as the height difference between the magma chamber and the eruptive vent increases because the magma column becomes much higher. Even though distal down-rift eruptions require a longer dike than summit eruptions, the static pressure of the magma in the eruption conduit required to erupt at a summit ~1 km higher than the distal end of the rift is ~30 MPa greater, whereas viscous flow and thermal dissapation in a ~20 km long magma conduit requires only ~3 MPa greater pressure than for a ~1 km long conduit [*Hardee*, 1987]. Yet, our observations of the EPR crest indicate that the eruptions with the lowest inferred effusion rates most often occur at the distal ends of the volcanic segments.

The reason why the eruption effusion rate seen along the EPR tends to be lower, instead of higher, at the distal ends of volcanic segments is that the topographic rise at the EPR is not a volcanic edifice at all, but rather is an isostatic or flexural feature [*Eberle and Forsyth*, 1998; *Madsen et al.*, 1986]. The crust thickens rapidly away from the ridge axis but changes little along-axis [*Carbotte and Macdonald*, 1994; *Harding et al.*, 1993]. As a consequence, the height of the magma column is not directly related to the elevation of the eruptive vent. The driving pressure for the eruption, ΔP, equals the difference between the ambient pressure on the magma source plus any magma overpressure, and the weight of the magma in the eruption conduit plus the viscous forces hindering magma flow. For the small length scales of diking (<10 km) and the relatively low lava viscosity of basaltic melt, the effects of viscous dissipation and conductive cooling are negligible so long as the driving pressure

exceeds 10^{-2} MPa [*Rubin*, 1995]. The driving pressure, ΔP, of an eruption from a dike on the EPR fed from the AMC may be simplified to an analytic equation:

$$\Delta P = \rho_c gZ + \Delta P_m - \rho_m gZ - \gamma Z \qquad (1)$$

where ρ_c is the bulk density of the overlying crust, ρ_m is the density of the magma, g is the gravitational acceleration, Z is the depth to the AMC, ΔP_m is the overpressure in the magma chamber, and γ is the dynamic pressure required to drive magma up the dike [*Buck et al.*, 1997; *Jaupart*, 2000]. *Buck et al.* [1997] found that the extrusive:intrusive thickness ratio above the AMC was self-regulating to keep the bulk density of overlying crust close to the magma density, effectively canceling the first and third terms of equation 1. This is fundamentally different from volcanic systems that build a central volcano edifice.

In light of the limited range of axial depth in our study area, we might expect that not much variation in effusion rates would be observed. The high percentage of area covered by lobate lava flows throughout the study area implies that eruption effusion rates are reasonably uniform. However, when eruptions of lower or higher inferred effusion rates do occur they most often do so at volcanic segment ends or centers, respectively (Figure 9). We are still left with the question: why do volcanic effusion rates correlate with the ridge structural segmentation?

Magmatic overpressure in the AMC is likely to be the main factor controlling mid-ocean ridge eruptions. Changes in magmatic overpressure on the EPR have never been measured directly. This underscores the need for detailed geodetic measurements that could detect changes in the state of the AMC over time. The pressure required to push magma up the dike against viscous resistance to flow, γZ in equation 1, is probably ~1 MPa when Z is ~1.5 km, but also is inversely related to dike width for a Bingham magma rheology [*Buck et al.*, 1997; *Hardee*, 1987]. We speculate that magma overpressure within an order of magnitude of ~1 MPa might be sufficient to initiate an eruption, if dikes follow preexisting fissures most of the way to the surface. Changes in the depth of the AMC below the seafloor of ~100 m will only change γZ by <0.1 MPa for a 1 m wide dike. We neglect the fracture toughness of the overlying crust in this calculation because the role of crustal fissuring in dike injection and eruption is unknown.

Dike width may be the critical factor controlling eruption effusion rate, such that wider dikes are expected to produce higher lava effusion rates [*Head et al.*, 1996]. The eruption effusion rate from a long fissure per unit length of the fissure, Q, is related to dike width, W, by

$$Q = W^3 \Delta P / 12v \qquad (2)$$

where v is lava viscosity [*Head et al.*, 1996]. *Gregg and Fink* [1995] found a linear relationship between viscosity and effusion rate that would reasonably model the transition between different lava morphology types found on mid-ocean ridges. Assuming a basaltic viscosity between 100 Pa s [*Gregg et al.*, 1996] and 300 Pa s [*Head et al.*, 1996], we determine the approximate effusion rate for the pillow-lobate and lobate-sheet transitions from *Gregg and Fink* [1995] as 10^1 m^3/s and 10^3 m^3/s respectively. We then use equation 2 to calculate the relationship between dike width and driving pressure (Figure 12). Although we have limited constraints on the process, the driving pressure for eruptions, ΔP, is likely to be within an order of magnitude of 1 MPa based on our earlier estimates. In the range of magmatic driving pressures of 0.1-1 MPa, changing the dike width from 0.5 m to 2 m could produce a corresponding change in lava morphology from pillow to sheet lava flows (Figure 12). These are also the range of dike widths most commonly seen in analogue crustal sections [*Karson*, 1998; *Karson et al.*, 1992; *Karson et al.*, 1999].

Near segment centers, especially within the ASCT, eruptions produce few to no pillow lava flows. Perhaps the reason is that wide dikes are common near volcanic segment centers, and that eruptions with <0.1 MPa driving pressure catastrophically and suddenly cease due to reaching the threshold for viscous transport in the magma column before generating low effusion rate pillow flows. For example, the driving pressure must fall well below 0.1 MPa for a 2 m wide dike to erupt pillow flows (Figure 12). The tendency for flows to focus along fissures is not a linear process, but may be enhanced where thinner dikes lead to increased cooling of magma during transport, raising magma viscosity, and simultaneously increasing viscous resistance to magma flow [*Rubin*, 1995; *Wylie et al.*, 1999]. Thus, wide (~2 m) dikes near segment center may be able to maintain high effusion rates throughout an eruption. In contrast, initially narrower (<1 m) dikes at volcanic segment ends may focus more quickly to point sources, further reducing the eruption effusion rate.

Factors controlling eruption effusion rate (pressure and viscosity of magma within the dike, and dike width) are ultimately controlled by the magma source and the path of the dike from source to seafloor surface. The seismic (Table 1) and geochemical (Figure 10) evidence is consistent with a smaller volume, lower temperature, poorly interconnected magma plumbing system near third-order segment boundaries at the level of the AMC. We envision two scenarios for the volcanic plumbing system between the AMC and seafloor: segment-length dikes and short dikes (Figure 13). In one

scenario (Figure 13a), long dikes propagate along-axis and upward from volcanic segment centers, so that eruptions near the volcanic segment ends tend to come from the vicinity of the propagating tip. Thus, near the segment end, the dike is narrowest, the magma farthest-traveled, and low effusion rate eruptions are common. A propagating dike, similar to what we envision for the NEPR, was suggested to account for the high levels of hydrothermal activity near the center and the formation of pillow lava mounds at the end of the northern Cleft segment of the Juan de Fuca ridge [*Embley and Chadwick*, 1994]. In the other scenario (Figure 13b), dikes are much smaller in along-axis length and do not propagate along-axis. In the case of short along-axis dikes (Figure 13b), narrower dikes, lower magma driving pressure, and higher magma viscosity are all consistent with eruption from the smaller, cooler magma source expected near a volcanic segment end.

The decreasing average volcanic effusion rate approaching the ends of third-order segments and the nearly constant average thickness of the volcanic layer (measured by the thickness of seismic layer 2A [*Harding et al.*, 1993]) together imply that eruptions must be longer-lived or more frequent near volcanic segment ends than segment centers. We speculate that the thickness of the low density volcanic layer may control the local eruption location and longevity [e.g., *Buck et al.*, 1997]. This requires that buoyancy forces as well as crack propagation due to internal magma pressure control the ascent of the dike. Possibly, buoyancy becomes more important in the later stages of the dike propagation or when magma pressure is otherwise low. Then, the dike will propagate along the base of the volcanic layer until it reaches a location where the volcanic layer is thin enough that the dike may penetrate to the surface (Figure 13a-2). This could allow low effusion rate eruptions to occur over longer periods or on shorter intervals in order to build a volcanic layer of uniform thickness along the crest of the EPR.

7. Conclusions

Several new conclusions about the nature of volcanic systems at fast-spreading ridges result from this study of the distribution of volcanic structures and lava flow morphology on the EPR.

1. The third-order ridge discontinuities in the axial bathymetry correspond to areas along the ridge axis where volcanic structures (axial lava domes and breaks in the ASCT) and lava flow morphology (increased abundance of pillow lava flows) indicate that eruption effusion rates have been reduced. We infer that the reduction in eruption effusion rates is due to a disruption in the volcanic plumbing system delivering lava to the eruptive vent.

2. Consistent patterns in the lava dome and lava morphology distribution in the axial zone emerge when multiple third-order segments are stacked to average their random variations in space and time. These patterns suggest that volcanic segmentation is far more persistent than individual eruptive episodes.
3. Volcanic systems segmented by third-order discontinuities are estimated to last 10^4-10^5 yrs., one to three orders of magnitude longer than hydrothermal systems segmented by fourth-order discontinuities [*Haymon*, 1996] that last 10^2-10^3 yrs.
4. We infer that the volcanic segmentation is influenced directly by segmentation of magma supply at shallow crustal levels. The structure of the AMC and along-axis geochemical variations correlate with volcanic segmentation.
5. No volcanic segment boundaries exist where the ASCT is a continuous structure. However, two gaps in the ASCT (the fissure-cut relay zone at 9°43.5'-45'N and the overlapping troughs around 9°37'N) correspond to volcanic segment boundaries.
6. Volcanic segmentation corresponds to third-order ridge segmentation on both the northern and southern EPR. The distribution of volcanic structures and lava flow morphology observed on both the northern and southern EPR implies that decreased eruption effusion rates near third-order segment ends is characteristic of fast-spreading ridges.
7. Axial pillow lava domes at 9°-10°N are rare in comparison to the southern EPR [*White et al.*, 2000]. However, the few lava domes that exist at 9°-10°N are closely associated with volcanic segment ends.
8. Pillow lava flows are nearly twice as abundant on the EPR at 9°-10°N and at 17°-18°S [*White et al.*, 2000] as previously thought for fast-spreading ridges [*Bonatti and Harrison*, 1988], but their distribution is strongly concentrated toward ridge discontinuities.
9. Lobate lava flows are most common lava morphology on both the northern and southern EPR, but regional variations in the abundance of sheet flows and pillow flows are important indicators of the variation in volcanic effusion rate.

References

Auzende, J.M., V. Ballu, R. Batiza, D. Bideau, J.L. Charlou, M.-H. Cormier, Y. Fouquet, P. Geistdoerfor, Y. Lagabrielle, J. Sinton, and P. Spadea, Recent tectonic, magmatic and hydrothermal activity on the East Pacific Rise between 17° and 19°S: Submersible observations, *J. Geophys. Res.*, *101* (B8), 17,995-18,010, 1996.

Basaltic-Volcanism-Study-Project, Basaltic Volcanism on the Terrestrial Planets, pp. 1286, Pergamon Press, New York, 1981.

Batiza, R., and Y. Niu, Petrology and magma chamber processes at the East Pacific Rise ~9°30'N, *J. Geophys. Res.*, *97* (B5), 6779-6797, 1992.

Bonatti, E., and C.G.A. Harrison, Eruption style of basalt in oceanic spreading ridges and seamounts: Effect of magma temperature and viscosity, *J. Geophys. Res.*, *93* (B4), 2967-2980, 1988.

Buck, W.R., S.M. Carbotte, and C. Mutter, Controls on extrusion at mid-ocean ridges, *Geology*, *25* (10), 935-938, 1997.

Carbotte, S.M., and K.C. Macdonald, The axial topographic high at intermediate and fast spreading ridges, *Earth Planet. Sci. Lett.*, *128*, 85-97, 1994.

Carbotte, S.M., A. Solomon, and G. Ponce-Correa, Evaluation of morphological indicators of magma supply and segmentation from a seismic reflection study of the East Pacific Rise, 15 30'-17 N, *J. Geophys. Res.*, *105* (B2), 2737-2760, 2000.

Cochran, J.R., D.J. Fornari, B.J. Coakley, R. Herr, and M.A. Tivey, Continuous near-bottom gravity measurements made with a BGM-3 gravimeter in DSV Alvin on the East Pacific Rise near 9 degree 31' N and 9 degrees 50'N, *J. Geophys. Res.*, *104*, 10,841-10,861, 1999.

Cormier, M.-H., D.S. Scheirer, and K.C. Macdonald, Evolution of the East Pacific Rise at 16°-19°S since 5 Ma: Bisection of OSC's by new rapidly propagating ridge segments, *Mar. Geophys. Res*, *18* (1), 52-84, 1996.

Detrick, R.S., P. Buhl, E. Vera, J. Mutter, J. Orcutt, J. Madsen, and T. Brocher, Multi-channel seismic imaging of a crustal magma chamber along the East Pacific Rise, *Nature*, *326*, 35-41, 1987.

Dunn, R.A., D.R. Toomey, and S.C. Solomon, Three-dimensional seismic structure and physical properties of the crust and shallow mantle beneath the East Pacific Rise at 9 30'N, *J. Geophys. Res.*, *105*, 23,537-23,556, 2000.

Eberle, M.A., and D.W. Forsyth, An alternative dynamic model of the axial topographic high at fast spreading ridges, *J. Geophys. Res.*, *103*, 12,309-12,320, 1998.

Embley, R.W., and W.W. Chadwick, Volcanic and hydrothermal processes associated with a recent phase of seafloor spreading at the northern Cleft segment: Juan de Fuca Ridge, *J. Geophys. Res.*, *99*, 4741-4760, 1994.

Embley, R.W., W.W. Chadwick, M.R. Perfit, M.C. Smith, and J.R. Delaney, Recent eruptions on the CoAxial segment of the Juan de Fuca ridge: Implications for mid-ocean ridge accretion processes, *J. Geophys. Res.*, *105* (B7), 16,501-16,526, 2000.

Engles, J., M. Edwards, D. Fornari, G. Kurras, and D. Bohnensteihl, Crustal porosity and lava distribution systems at a small overlapping spreading center on the East Pacific Rise, 9 37'N, *Eos, Trans. AGU*, *81* (48 (Fall Meet. Suppl.)), F1076, 2000.

Epp, D., R.W. Decker, and A.T. Okamura, Relation of summit deformation to East Rift Zone eruptions on Kilauea Volcano, Hawai'i, *Geophys. Res. Lett.*, *10*, 493-496, 1983.

Fornari, D., M. Perfit, M. Tolstoy, R. Haymon, D. Scheirer, P. Johnson, G. Kurras, S. White, and J. Getsiv, AHA-NEMO2, Shipboard data web site compiled during R/V Melville NEMO Expedition, Leg 2, WHOI, 2000.

Fornari, D.J., R.M. Haymon, M.R. Perfit, T.K.P. Gregg, and M.H. Edwards, Axial summit trough of the East Pacific Rise 9°N to 10°N: Geological characteristics and evolution of the axial zone on fast-spreading mid-ocean ridges, *J. Geophys. Res.*, *103* (B5), 9827-9855, 1998.

Gente, P., J.M. Auzende, V. Renare, Y. Fouquet, and D. Bideau, Detailed geological mapping by submersible of the East Pacific Rise axial graben near 13°N, *Earth. Planet. Sci. Lett.*, *78*, 224-236, 1986.

Gregg, T., and W. Chadwick, Submarine lava-flow inflation; a model for the formation of lava pillars, *Geology*, *24* (11), 981-984, 1996.

Gregg, T.K.P., and J.H. Fink, Quantification of submarine lava-flow morphology through analog experiments, *Geology*, *23*, 73-76, 1995.

Gregg, T.K.P., D.J. Fornari, M.R. Perfit, R.M. Haymon, and J.H. Fink, Rapid emplacement of a mid-ocean ridge lava flow on the East Pacific Rise at 9 degrees 46'-51' N, *EPSL*, *144* (3-4), E1-E7, 1996.

Griffiths, R.W., and J.A. Fink, Solidification and morphology of submarine lavas; a dependence on extrusion rate, *J. Geophys. Res.*, *97* (B13), 19729-19737, 1992.

Gudmundsson, A., Infrastructure and mechanics of volcanic systems in Iceland, *J. Volcanol. Geotherm. Res.*, *64*, 1-22, 1995.

Hardee, H.C., Heat and mass transport in the east-rift-zone magma conduit of Kilauea Volcano, in *Volcanism in Hawaii*,, edited by R.W. Decker, T.L. Wright, and P.H. Stauffer, pp. 1471-1486, 1987.

Harding, A.J., G.M. Kent, and J.A. Orcutt, A multichannel seismic investigation of upper crustal structure at 9°N on the East Pacific Rise: Implications for crustal accretion, *J. Geophys. Res.*, *98*, 13925-13944, 1993.

Haymon, R., The response of ridge-crest hydrothermal sytems to segmented, epispdic magma supply, in *Tectonic, Magmatic, Hydrothermal and Biological Segmentation of Mid-Ocean Ridges*, edited by C.J. MacLeod, P.A. Tyler, and C.L. Walker, pp. 157-168, Geologcial Society Special Publication, 1996.

Haymon, R.M., and, and others, Volcanic eruption of the mid-ocean ridge along the East Pacific Rise crest at 9°45'-52'N: Direct submersible observations of seafloor phenomena associated with an eruption event in April, 1991, *Earth Planet. Sci. Lett.*, *119*, 85-101, 1993.

Haymon, R.M., D.J. Fornari, M.H. Edwards, S. Carbotte, D. Wright, and K.C. Macdonald, Hydrothermal vent distribution along the East Pacific Rise Crest (9°09'-54'N) and its relationship to magmatic and tectonic processes on fast-spreading mid-ocean ridges, *Earth Planet. Sci. Lett.*, *104*, 513-534, 1991.

Head, J.W., L. Wilson, and D.K. Smith, Mid-ocean ridge eruptive vent morphology and substructure: Evidence for dike widths, eruption rates, and the evolution of eruptions and axial volcanic ridges, *J. Geophys. Res.*, *101* (B12), 28,265-28,280, 1996.

Holcomb, R.T., Eruptive History and long-term behavior of Kilauea Volcano, in *Volcanism in Hawaii*, edited by R.W. Decker, T.L. Wright, and P.H. Stauffer, pp. 261-350, USGS, Reston, VA, 1987.

Holcomb, R.T., J.G. Moore, P.W. Lipman, and R.H. Belderson, Voluminous submarine lava flows from Hawaiian volcanoes, *Geology*, *16*, 400-404, 1988.

Jaupart, C., Magma ascent at shallow levels, in *Encyclopedia of Volcanoes*, edited by H. Sigurdsson, pp. 237-245, Academic Press, 2000.

Karson, J.A., Internal structure of oceanic lithosphere: A perspective from tectonic windows, in *Faulting and magmatism at mid-ocean ridges*, edited by P.T.D. W. R. Buck, J. A. Karson, Y. Lagabrielle, pp. 177-218, AGU, 1998.

Karson, J.A., S.D. Hurst, and P. Lonsdale, Tectonic rotations of dikes in fast-spread oceanic crust exposed near Hess Deep, *Geology*, *20* (8), 685-692, 1992.

Karson, J.A., E.M. Klein, S.D. Hurst, and H.D.S.P., Internal structure of uppermost fast-spread oceanic crust of the East Pacific Rise exposed at the Hess Deep rift: Results from Alvin, Argo II, and DSL-120 investigations, *Eos, Trans. AGU*, *80* (46 Fall Meet. Suppl.), F983, 1999.

Kastens, K.A., W.B.F. Ryan, and P.J. Fox, Structural and volcanic expression of a fast slipping ridge-transform-ridge-plate boundary: Sea MARC I and photographic surveys of the Clipperton Transform Fault, *J. Geophys. Res.*, *91* (B3), 3469-3488, 1986.

Kent, G., A.J. Harding, and J.A. Orcutt, Distribution of magma beneath the East Pacific Rise between the Clipperton Transform and the 9°17'N deval from forward modeling of common depth point data, *J. Geophys. Res.*, *98* (B8), 13,945-13,969, 1993a.

Kent, G., A.J. Harding, and J.A. Orcutt, Distribution of magma beneath the East Pacific Rise near the 9°03'N overlapping spreading center from forward modeling of CDP data, *J. Geophys. Res.*, *98*, 13,971-13,995, 1993b.

Kurras, G.J., D.F. Fornari, M.F. Edwards, M.R. Perfit, and M.C. Smith, Volcanic morphology of the East Pacific Rise crest 9 49'-52'N: Implications for volcanic emplacement processes at fast-spreading mid-ocean ridges, *Mar. Geophys. Res.*, *21*, 23-41, 2000.

Langmuir, C.H., J.F. Bender, and R. Batiza, Petrological and tectonic segmentation of the East Pacific Rise, 5°30'N-14°30'N, *Nature*, *322*, 422-429, 1986.

Lee, S.-M., S.C. Solomon, and M.A. Tivey, Fine-scale crustal magnetization anomalies and segmentation of the East Pacific rise, 9º10'-9º50'N, *J. Geophys. Res.*, *101*, 22,033-20,050, 1996.

Lonsdale, P., Geomorphological reconaissance of the submarine part of the East Rift Zone of Kilauea Volcano, Hawai'i, *Bull. Volcanol.*, *51* (2), 123-144, 1989.

Macdonald, K.C., and P.J. Fox, The axial summit graben and cross-sectional shape of the East Pacific Rise as indicators of axial magma chambers and recent volcanic eruptions, *Earth Planet. Sci. Lett.*, *88*, 119-131, 1988.

Macdonald, K.C., P.J. Fox, S. Carbotte, M. Eisen, S. Miller, L. Perram, D. Scheirer, S. Tighe, and C. Weiland, The East Pacific Rise and its flanks, 8°-18°N: History of segmentation, propagation and spreading direction based on SeaMARC II and Sea Beam studies, *Mar. Geophys. Res.*, *14*, 299-344, 1992.

Macdonald, K.C., P.J. Fox, L.J. Perram, M.F. Eisen, R.M. Haymon, S.P. Miller, S.M. Carbotte, M.-H. Cormier, and A.N. Shor, A new view of the mid-ocean ridge from the behaviour of ridge-axis discontinuities, *Nature*, *335* (6187), 217-225, 1988.

Macdonald, K.C., J.-C. Sempere, and P.J. Fox, East Pacific Rise from Siqueiros to Orozco Fracture Zones: Along-strike continuity of axial neovolcanic zone and structure and evolution of overlapping spreading centers, *J. Geophys. Res.*, *89* (B7), 6049-6069, 1984.

Madsen, J.A., R. Detrick, T. Brocker, P. Buhl, J. Mutter, and J. Orcutt, Variations in the morphology and isostasy of the East Pacific Rise between 9° and 14°N, *EOS Trans. AGU*, *67*, 360, 1986.

McConachy, T.F., R.D. Ballard, M.J. Mottl, and R.P. Von Herzen, Geologic form and setting of a hydrothermal vent field at lat 10°56’N, East Pacific Rise: A detailed study using ANGUS and ALVIN, *Geology*, *14*, 295-298, 1986.

Perfit, M.R., and W.W. Chadwick, Magmatism at mid-ocean ridges: constraints from volcanological and geochemical investigations, in *Faulting and magmatism at mid-ocean ridges*, edited by W.R. Buck, P.T. Delaney, J.A. Karson, and Y. Lagabrielle, pp. 59-116, AGU, Washington DC, 1998.

Perfit, M.R., D.J. Fornari, M.C. Smith, J.F. Bender, C.H. Langmuir, and R.M. Haymon, Small-scale spatial and temporal variations in mid-ocean ridge crest magmatic processes, *Geology*, *22*, 375-379, 1994.

Renard, V., R. Hekinian, J. Francheteau, R.D. Ballard, and H. Backer, Submersible observations at the axis of the ultra fast spreading East Pacific Rise (17°30' to 21°30’S), *Earth Planet. Sci. Lett.*, *88*, 339-353, 1985.

Rossi, M.J., Morphology and mechanism of eruption of postglacial shield volcanoes in Iceland, *Bull. Volc.*, *57* (7), 530-540, 1996.

Rubin, A.M., Propagation of magma-filled cracks, *Annu. Rev. Earth Planet. Sci.*, *23*, 287-336, 1995.

Scheirer, D.S., D.J. Fornari, S.E. Humphris, and S. Lerner, High-resolution seafloor mapping using the DSL-120 sonar system: Quantitative assessment of sidescan and phase-bathymetry data from the Lucky Strike segment of the Mid-Atlantic Ridge, *Mar. Geophys. Res.*, *21* (1), 121-142, 2000.

Scheirer, D.S., and K.C. Macdonald, Variation in cross-sectional area of the axial ridge along the East Pacific Rise: Evidence for the magamatic budget of a fast-spreading center, *J. Geophys. Res.*, *98*, 7871-7885, 1993.

Sigurdsson, H., and S.R.J. Sparks, Lateral magma flow within rifted Icelandic crust, *Nature, 274*, 126-130, 1978.

Simkin, T., and L. Siebert, Earth's volcanoes and eruptions: An overview, in *Encyclopedia of Volcanoes*, edited by H. Sigmundsson, pp. 249-262, Academic Press, San Diego, 2000.

Singh, S.C., G.M. Kent, J.S. Collier, A.J. Harding, and J.A. Orcutt, Melt to mush variations in crustal magma properties along the ridge crest at the southern East Pacific Rise, *Nature, 394*, 874-878, 1998.

Sinton, J.M., and R.S. Detrick, Mid-ocean ridge magma chambers, *J. Geophys. Res.*, *97* (B1), 197-216, 1992.

Smith, D.K., and J.R. Cann, Constructing the upper crust of the Mid-Atlantic Ridge: A reinterpretation based on the Puna Ridge, Kilauea Volcano, *J. Geophys. Res.*, *104*, 25,379-25,400, 1999.

Smith, D.K., J.R. Cann, M.E. Dougherty, J. Lin, S. Spencer, C. MacLeod, J. Keeton, E. McAllister, B. Brooks, R. Pascoe, and W. Robertson, Mid-Atlantic Ridge volcanism from deep-towed side-scan sonar images, 25-29N, *J. Volc. Geotherm. Res.*, *67*, 233-262, 1995.

Smith, M.C., M.R. Perfit, D.J. Fornari, W.I. Ridley, M.H. Edwards, G. Kurras, and K.L. Von Damm, Segmentation and magmatic processes at a fast spreading mid-ocean ridge: Detailed geochemistry and mapping of the East Pacific Rise crest at the 9 37'N OSC, *Geochem. Geophys. Geosys.*, 2001.

Stewart, K.W., D. Chu, S. Malik, S. Lerner, and H. Singh, Quantitative seafloor characterization using a bathymetric sidescan sonar, *Jour. Ocean. Engin.*, *19*, 599-610, 1994.

Toomey, D.R., S.C. Solomon, and G.M. Purdy, Tomographic imaging of the shallow crustal structure of the East Pacific Rise at 9°30'N, *J. Geophys. Res.*, *99*, 24135-24157, 1994.

Vera, E.E., and J.B. Diebold, Seismic imaging of oceanic layer 2A between 9°30'N and 10°N on the East Pacific Rise from two-ship wide-aperture profiles, *J. Geophys. Res.*, *99*, 3031-3041, 1994.

Von Damm, K.L., Chemistry of hydrothermal vent fluids from 9 -10 N, East Pacific Rise: "Time zero," the immediate posteruptive period, *J. Geophys. Res.*, *105* (B5), 11,203-11,222, 2000.

Von Damm, K.L., S.E. Oosting, R. Kozlowski, L.G. Buttermore, M.D. Lilley, E.J. Olson, and E. McLaughlin, Evolution of East Pacific Rise hydrothermal vent fluids following a volcanic eruption, *Nature*, *375*, 47-50, 1995.

White, S.M., K.C. Macdonald, and R.M. Haymon, Basaltic lava domes, lava lakes, and volcanic segmentation of the southern East Pacific Rise, *J. Geophys. Res.*, *105*, 23,519-23,536, 2000.

Wilcock, W.S.D., D.R. Toomey, G.M. Purdy, and S.C. Solomon, The renavigation of Sea Beam bathymetric data between 9° N and 10° N on the East Pacific Rise, *Mar. Geophys. Res.*, *15*, 1-12, 1993.

Williams, H., The history and character of volcanic domes, *Bull. Dept. Geol. Sci., Univ. Calif. Publ.*, *21*, 51-146, 1932.

Wright, D.J., R.M. Haymon, and D.J. Fornari, Crustal fissuring and its relationship to magmatic and hydrothermal processes on the East Pacific Rise crest (9º12' to 54'N), *J. Geophys. Res.*, *100*, 6097-6120, 1995a.

Wright, D.J., R.M. Haymon, and K.C. Macdonald, Breaking new ground: Estimates of crack depth along the axial zone of the East Pacific Rise (9º12'-54'N), *Earth Planet. Sci. lett.*, *134*, 441-457, 1995b.

Wylie, J.J., K.R. Helfrich, B. Dade, J.R. Lister, and J.F. Salzig, Flow localization in fissure eruptions, *Bull. Volcanol.*, *60*, 432-440, 1999.

Figure Captions

Figure 1. Map of the study area with bathymetry shown in shaded relief illuminated from the west. Arrows show the end-points of third-order (volcanic) segments and are angled so that southeast pointing arrows mark the north end of a segment, and northwest pointing arrows mark the south end of a segment. The areas between arrows are very small overlap zones between ridge axes. The axial summit collapse trough (ASCT) modified from *Haymon et al.* [1991] is outlined in black. The two largest offsets in the ASCT correspond to third-order segment ends. The limits of the DSL-120 sonar coverage area are outlined by solid black line. The pillow lava domes found in the axial zone (shown as small open circles) are found exclusively near the volcanic segment ends. Columns on the right show distribution of segments and their relation to hydrothermal activity. The left column shows the discontinuity zones between the third-order segments (indicated by brackets). In the middle column, the black boxes labeled "gap" show where no evidence for hydrothermal activity was seen with *Argo* in 1989 and black dots show where black smoker chimneys or smoke plumes were seen in 1989 [*Haymon et al.*, 1991]. The right column shows the fourth-order ridge segments in the 1989 *Argo* survey area [*Haymon et al.*, 1991]. *Haymon et al.* [1991] expressed uncertainty about the location of the F/G segment boundary as indicated by the dashed arrow. Most third-order segments contain multiple fourth-order segments.

Figure 2. Map of the overlapping axial summit collapse troughs (ASCTs) that form a third-order segment boundary. Backscatter imagery is shown on the left panel, and the axial pillow lava domes are circled in black. This area was imaged by two overlapping axis-parallel swaths and one perpendicular swath. The right panel shows the 1989 *Argo* track in bold black lines, the ASCT modified from *Haymon et al.* [1991] in stipple fill, and pillow lavas identified from *Alvin* observations as small circles [*Smith et al.*, 2001]. The axial lava domes form near and extend to the south of the eastern ASCT limb. Note that most of the pillow lava observations from *Smith et al.* [2001] were outside the 1989 *Argo* coverage. The pillow domes correspond to the locations of pillow lava flows where they have been mapped visually by *Smith et al.* [2001].

Figure 3. Pillow lava domes, circled, found at a third-order segment end. The left panel shows the DSL-120 backscatter imagery. The right panel shows the DSL-120 phase bathymetry contoured at a 5 m interval. Locations of pillow lava domes are circled on both panels. Most domes have a hemispherical to semi-ellipsoidal shape, typical for lava domes.

Figure 4. DSL-120 backscatter imagery (left panel) and phase-bathymetry contoured at 5m interval (right panel) showing three lava mounds, circled by black lines, that appear to be cut by a fault, indicated by a dashed line. Low-intensity backscatter (dark) indicates the fault is down-dropped to the east. The ridge axis runs through the far western edge of the DSL-120 swath.

Figure 5. Plot of the height and radius for all of the pillow mounds within the study area indicating their shape is similar to lava domes. The radius of the dome was calculated as its basal perimeter divided by 2π with error bars showing 10% error based on our ability to measure mound radii by this method. The height error bars show an error of 5 m. The lines show the least-squares linear regression best-fit to the height:radius ratio of small Icelandic lava shields (h=0.038r) [*Rossi*, 1996] and axial pillow lava domes on the southern East Pacific Rise (SEPR) (h=0.2r) [*White et al.*, 2000]. These pillow constructions are too small and steep to be classified as lava shields, but are very similar to the SEPR lava domes.

Figure 6. The depth of the ridge axis within our study area shown at nearly 100X vertical exaggeration, has a small (<100 m) depth variation (top panel). The abundance of pillow lava domes in the axial zone (<500 m from the ridge axis) plotted by latitude in 2' (~4 km) bins (bottom panel). The total number of domes is shown by vertical columns, and the total basal area of the lava domes is shown by black dots. The areas where the most lava domes are located correspond very well to the bins where the third-order segment ends are located, shown by black arrows. Comparison of the axial depth to the lava domes illustrates that depth anomalies do not determine the third-order segment boundaries or the locations of lava domes.

Figure 7. The atypical third-order segment boundary zone at 9°44.8'N has widespread areas of small collapse pits unusual for third-order segment boundaries, although a high abundance of pillow lava is found here. The DSL-120 backscatter imagery (panel a) shows the *en echelon* fissures that form a relay zone between two axial collapse troughs. The ridge axis step right a total of 500 m through this fissure zone. The paired light-dark reflectors are fissures. The SeaBeam 2000 bathymetry [*Cochran et al.*, 1999] with a 10 m color change interval on the axial high (panel b) illustrates the right-lateral offset and a pinching of the width of the axial high at this ridge discontinuity.

Figure 8. Histogram plot of the lava morphology distribution from *Argo* observations in 1989 along the axial zone (<500 m from the ridge axis) plotted in 2' (~4 km) latitude bins. The relative abundance of each flow morphology is shown as a fraction of the seafloor imaged in the *Argo* survey for each bin,

so that all three panels will sum to 1. Darker fill in the columns indicates observations outside the axial summit collapse trough (ASCT), while lighter fill indicates observations made within the ASCT. Almost no pillow lava was found within the ASCT. The hashed lines indicate the third-order (volcanic) segment discontinuity zones from Figure 1. All third-order discontinuities correspond to local maxima in the abundance of pillow lava, and sheet flows are most abundant near mid-segment.

Figure 9. Histogram of (a) the total number of pillow lava domes and (b) the relative abundance of each class of lava morphology in the axial zone for all of the segments combined. The bin interval is normalized to 20% of the distance from the end to center of each segment in order to adjust for varying segment length. The total basal area of the lava domes in each bin is shown as black dots connected by lines. Pillow lava domes are most abundant and cover a greater area of seafloor near the segment ends in the bin at the third-order segment end. Lobate lava flows are consistently more abundant than either pillow or sheet lava flows alone. Lobate flows may be described as those flows not bulbous enough to be pillows nor flat enough to be sheet flows. Pillow lava is more than twice as abundant at the segment end as it is near segment centers, and sheet lava flows have the reverse relationship to segmentation. From this, we infer that lower eruption effusion rates are more typical of eruptions near the ends of third-order segments, producing the pillow lava domes there. This data is one line of evidence that the third-order segments correspond to individual volcanic sytems along the EPR.

Figure 10. Comparison of third-order segmentation to Mg# of the glass samples from microprobe analysis of volcanic glass on all of the rock samples collected in our study area by *Alvin*. The line is a step function showing the minimum Mg# every 3.7 km (2') along axis, the same bin interval used for the histograms in Figure 6 and 8. The hashed lines mark the third-order segment discontinuity zones (from Figure 1). Within third-order segments the minimum Mg# lowest values are found in the discontinuity zones. Also, there is more heterogeneity near segment ends. This is consistent with the morpho-structural and seismic data suggesting that the volcanic systems are disrupted at third-order discontinuities.

Figure 11. The fissure width in the axial zone (<500 m from the ridge axis) for each fissure crossing from *Argo* observations in 1989 [*Wright et al.*, 1995a]. The average fissure width (solid line) and maximum fissure width (dashed line) are plotted by latitude in 2' (~4 km) bins. The maximum observed fissure widths are constrained by the field-of-view of the *Argo* cameras to be less than ~8 m

wide [*Wright et al.*, 1995a]. The hashed lines mark the third-order segment discontinuity zones (from Figure 1). The bins with the highest maximum fissure width within each third-order segment are consistently found outside the discontinuity zones, except where fresh lava flows cover most axial fissures. The average fissure width is generally higher outside the discontinuity zones, but the large number of <1 m wide fissures south of 9°35'N complicate this trend. Pillow lava domes are more abundant in the areas where average fissure width is ~1 m.

Figure 12. The driving pressure at the volcanic vent needed to erupt a lava morphology for a geologically reasonable range of feeder dike widths. The divisions between pillow, lobate, and sheet flows are based on effusion rates of 100 Pa s (dashed line) and 300 Pa s (solid line) basalt during a fissure eruption for transitions between lava morphologies from *Gregg and Fink* [1995]. The prevalence of lobate lava in the study area is reasonable for dike widths of 1-2 m and driving pressures of ~1 MPa. Dikes narrower than ~1 m have a much greater tendency to erupt pillow lava.

Figure 13. Conceptual models of along-strike dike propagation within half of a volcanic segment that could explain the trends observed in volcanic structures along the ridge crest. The essential difference between these models is that a long dike narrows toward the segment end as it tapers to zero width (A), and short dikes are narrower if they originate near the volcanic segment end and are wider near segment center where the AMC is inferred to be more robust (B). The depth to the volcanic layer, sheeted dike layer, and axial magma chamber (AMC) are averaged from seismic measurements [*Detrick et al.*, 1987; *Harding et al.*, 1993]. The top model (A) shows a three panel time sequence of dike initiation near the volcanic segment center (A0), dike propagation along-strike and upwards (A1), and finally eruption with some near-surface segmentation within the dike (A2). The long dike (A) tapers toward the propagating tip, resulting in a narrower width, and consequently lower effusion rate eruptions, near segment ends than the dike initiation point near segment center. At the end of the propagation (A2), a magma conduit forms at the base of the extrusive layer and propagates to the end of the segment, providing a mechanism for longer-lived eruptions where effusion rates are lower near the ends of volcanic segments (see text for discussion). The alternate model (B) shows the development of short along-axis dikes that do not propagate significantly along-axis, and most magma flow is vertical instead. The two scenarios represent end-members of the style of eruptive dikes feeding eruptions on the EPR that would account for the trend toward lower eruption effusion rates near volcanic segment ends than near centers.

Table 1. Endpoints of the third-order ridge axis discontinuities (latitudes rounded to nearest 0.1') offsets picked initially from ridge axis offsets and saddles visible in multibeam bathymetry 10m contour maps to nearest 1', then refined to nearest 0.1' from DSL-120 sidescan sonar data, the use of supporting data is independent of offsets picked on this table

Latitude *(*distance south of previous offset*)*	***Longitude***	*Size and Sense of Offset on Multibeam bathymetry maps (100m grid, 10m contours), and DSL-120 bathymetry maps (4m grid, 5m contours)*	*How Offsets Were Previously Noted*	*Seismic AMC discontinuity*
9°57.2'N	**104°18.5'W**	Multibeam: bathymetric saddle point (-20m) DSL-120: 15-20 m deep saddle without distinct lateral offset, location of ridge axis imprecise ±250 m		break (Detrick et al., 1987; Vera and Diebold, 1994)
9°44.8'N (23.4 km)	**104°16.5'W**	Multibeam: 0.5 km right offset of axis through Saddle Point (-10m) DSL-120: 0.3-0.5 km right translation of axis from a ~50m wide, ~20m deep ASCT at 9°45'N through a zone of right-stepping en echelon fissures that merge into a ~400m wide, ~20m deep ASCT at 9°43.5'N	ASCT becomes zone of fissures, (Haymon et al., 1991) 0.5 km right-step in SeaMarc II, part of en echelon series of offsets, (Macdonald et al., 1992)	pinch-down in width, depth increase (Kent et al., 1993a)
9°37.9'N **9°36.4'N** (15.3 km)	**104°13.9'W** **104°15.2'W**	Multibeam: 0.5 km right step of axis, no depth change DSL120: <0.5 km right step without depth change, between 2 overlapping ~200m wide, ~20m deep ASCT's	Several en echelon offsets of ASCT from SeaMarcII, (Macdonald et al., 1992) ASCT overlap, (Haymon et al., 1991)	pinch-down, possible break (Kent et al., 1993a; Toomey et al., 1990)
9°21.0'N **9°19.7'N** (31.5 km)	**104°13.3'W** **104°12.9'W**	Multibeam: ~1 km right stepping overlap of <10 m topographic highs marking axes DSL-120: >0.5 km right stepping overlap of local topographic high (20m) from south and >200m wide zone of fissures and collapses from north	1 km right-step, (Macdonald et al., 1992) possible 4th order offset and lava-age transition boundary, (Haymon et al., 1991)	MCS off axis width discontinuty across offset - double reflection? (Kent et al., 1993b)
9°12.0'N **9°10.4'N** (19.4 km)	**104°13.1'W** **104°12.6'W**	Multibeam: 0.5 km right offset of axis through saddle point (-20m) DSL120: 0.5 km right stepping overlap of two local topographic ridges (200-400m wide, >30m high)	0.5 km right-step, (Macdonald et al., 1992) possible 4th order offset (Haymon et al., 1991)	break in AMC (Detrick et al., 1987; Kent et al., 1993b)
9°03'N (16.8 km)	**104°12'W**	Multibeam: southern tip of east limb DSL-120: no coverage available	10 km right-step overlapping offset (Macdonald et al., 1992)	break in AMC (Detrick et al., 1987; Kent et al., 1993b)

Table 2. Visual coverage of the *Argo* survey tracklines within a corridor of specified width about the ridge axis. Coverage within 500 m was used to determine the lava morphology in this study.

Maximum Distance from Ridge Axis in corridor	seafloor imaged as percent of total seafloor within corridor	km^2 of seafloor imaged
100 m	34%	2.58
250 m	23%	4.30
500 m	14%	5.50

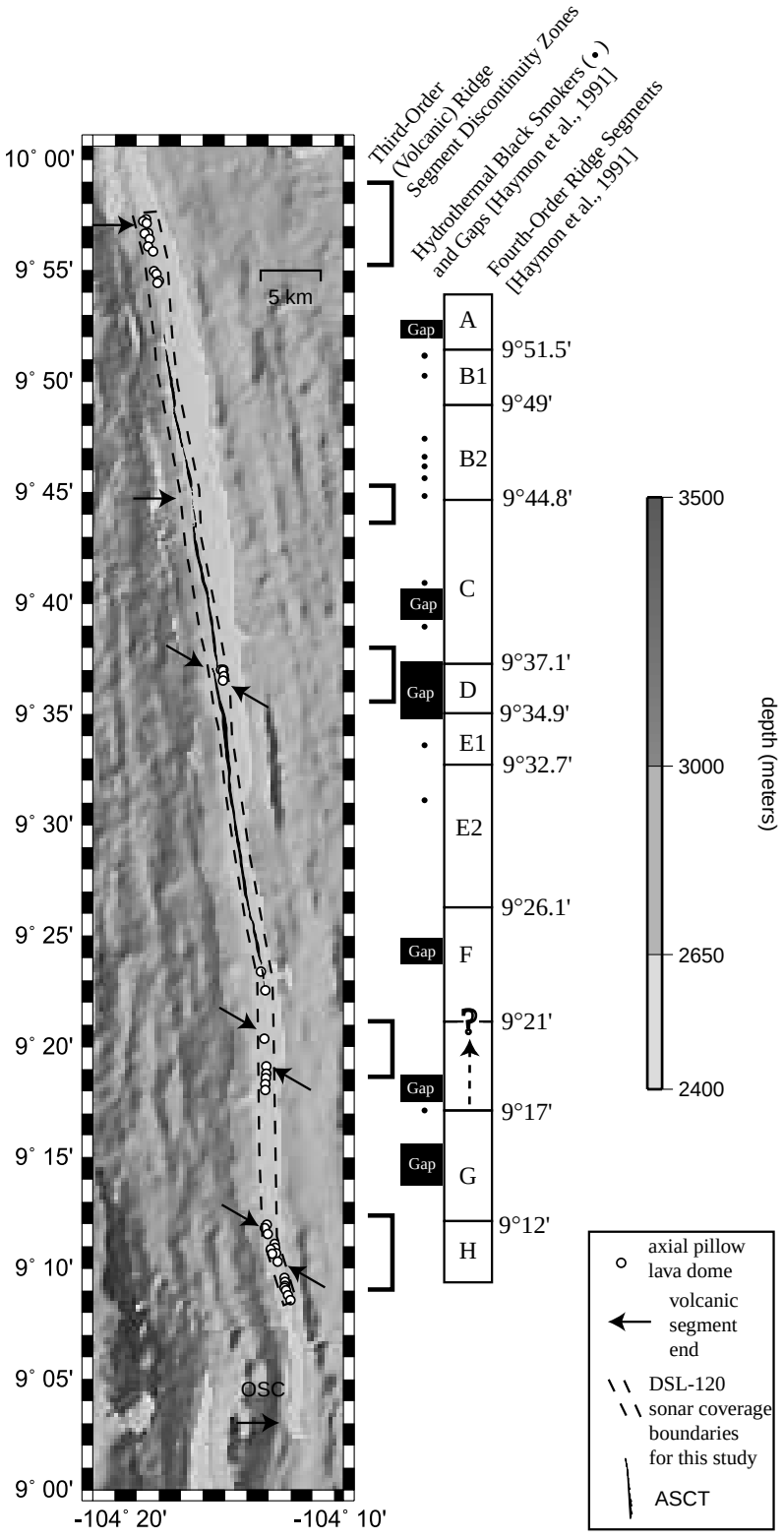
Third-Order (Volcanic) Ridge Segment Discontinuity Zones
Hydrothermal Black Smokers (•) and Gaps [Haymon et al., 1991]
Fourth-Order Ridge Segments [Haymon et al., 1991]
10˚ 00'
9˚ 55'
9˚ 50'
9˚ 45'
9˚ 40'
9˚ 35'
9˚ 30'
9˚ 25'
9˚ 20'
9˚ 15'
9˚ 10'
9˚ 05'
9˚ 00'
-104˚ 20'
-104˚ 10'
5 km
OSC
Gap
A
B1
B2
C
D
E1
E2
F
G
H
9°51.5'
9°49'
9°44.8'
9°37.1'
9°34.9'
9°32.7'
9°26.1'
9°21'
9°17'
9°12'
?
3500
3000
2650
2400
depth (meters)
axial pillow lava dome
volcanic segment end
DSL-120 sonar coverage boundaries for this study
ASCT

Figure 1

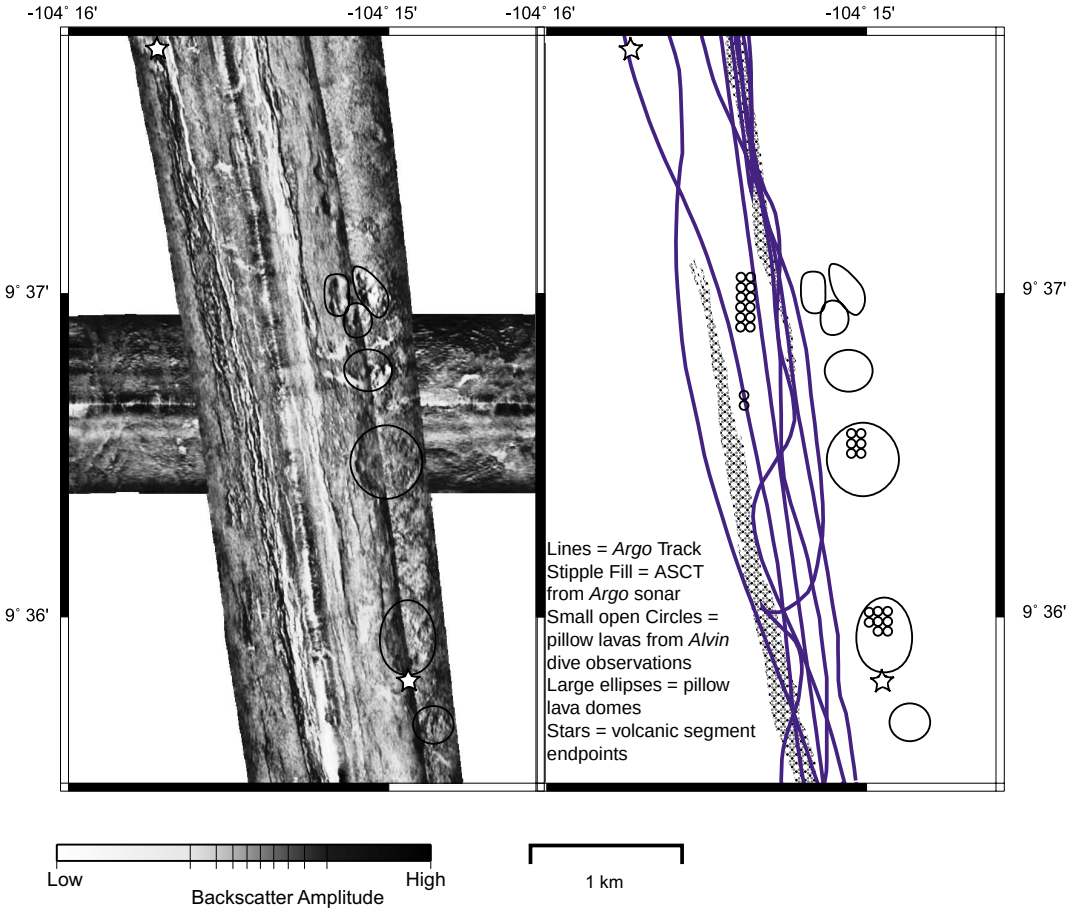
-104˚ 16'
-104˚ 15'
-104˚ 16'
-104˚ 15'
9˚ 37'
9˚ 36'
9˚ 37'
9˚ 36'
Lines = *Argo* Track
Stipple Fill = ASCT from *Argo* sonar
Small open Circles = pillow lavas from *Alvin* dive observations
Large ellipses = pillow lava domes
Stars = volcanic segment endpoints
Low
High
Backscatter Amplitude
1 km

Figure 2

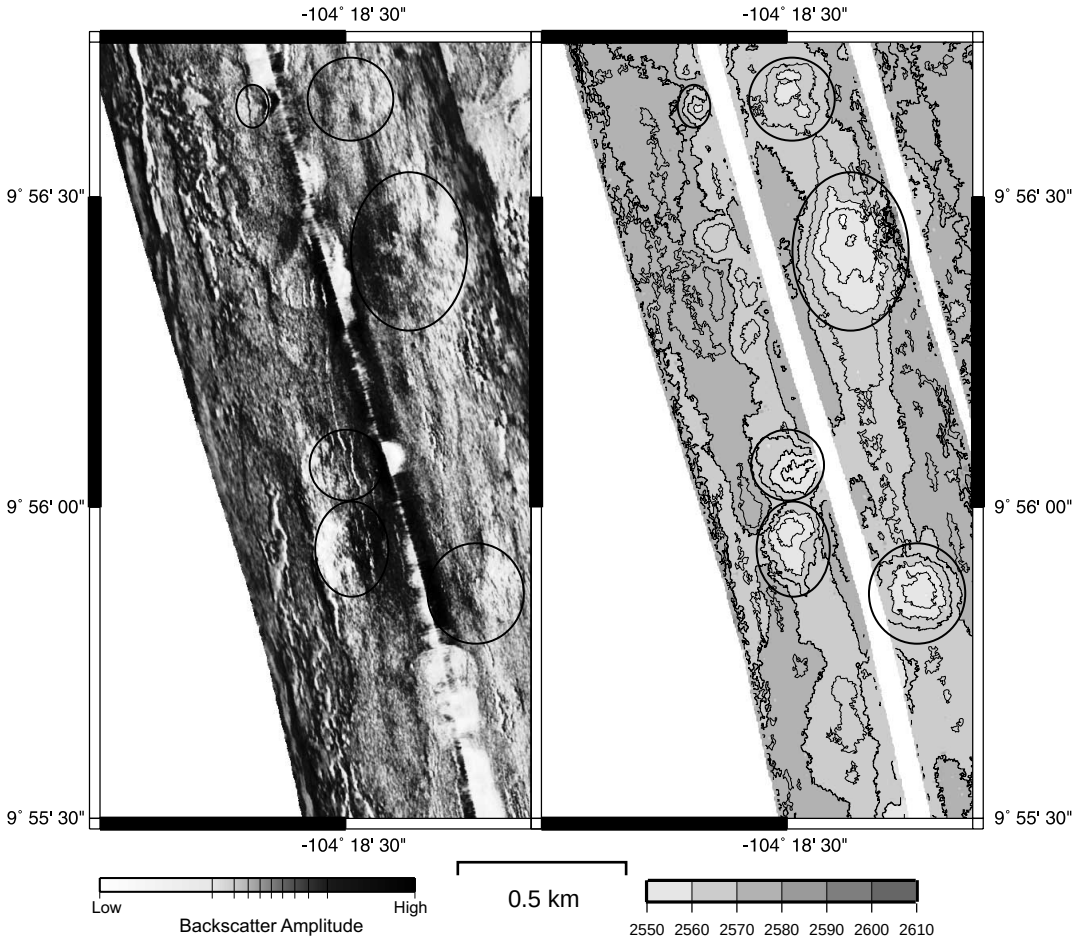
-104˚ 18' 30"
-104˚ 18' 30"
9˚ 56' 30"
9˚ 56' 30"
9˚ 56' 00"
9˚ 56' 00"
9˚ 55' 30"
9˚ 55' 30"
-104˚ 18' 30"
-104˚ 18' 30"
Low
High
Backscatter Amplitude
0.5 km
2550 2560 2570 2580 2590 2600 2610

Figure 3

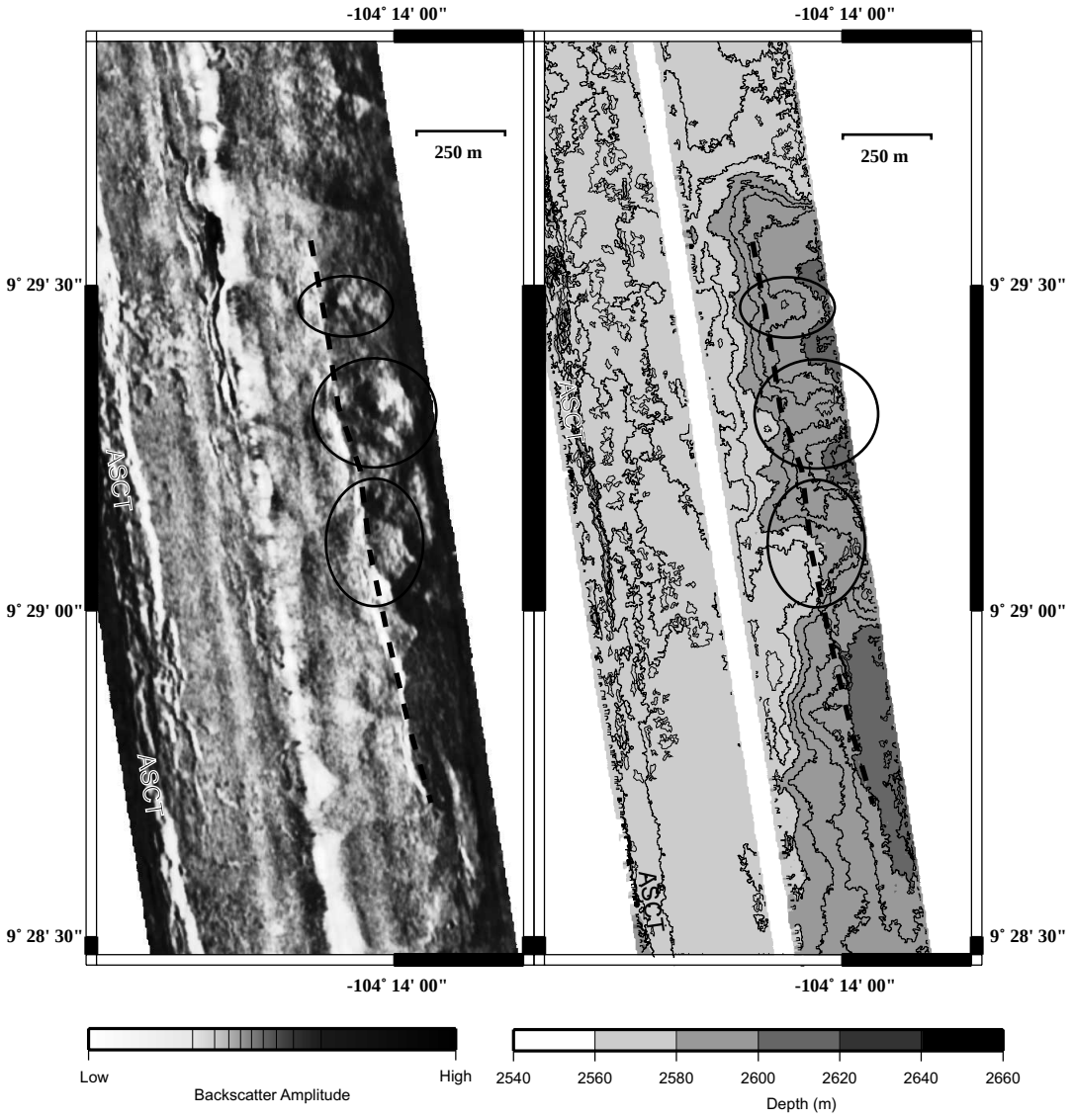
-104˚ 14' 00"
-104˚ 14' 00"
250 m
250 m
9˚ 29' 30"
9˚ 29' 00"
9˚ 28' 30"
ASCT
ASCT
ASCT
ASCT
-104˚ 14' 00"
-104˚ 14' 00"
Low
High
Backscatter Amplitude
2540
2560
2580
2600
2620
2640
2660
Depth (m)

Figure 4

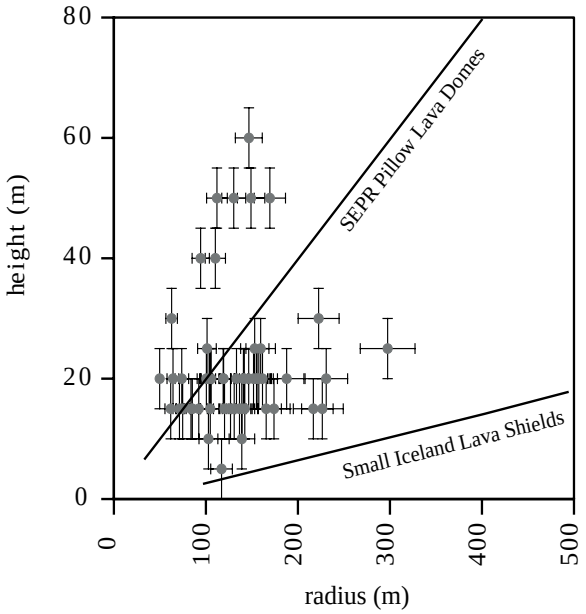

Figure 5

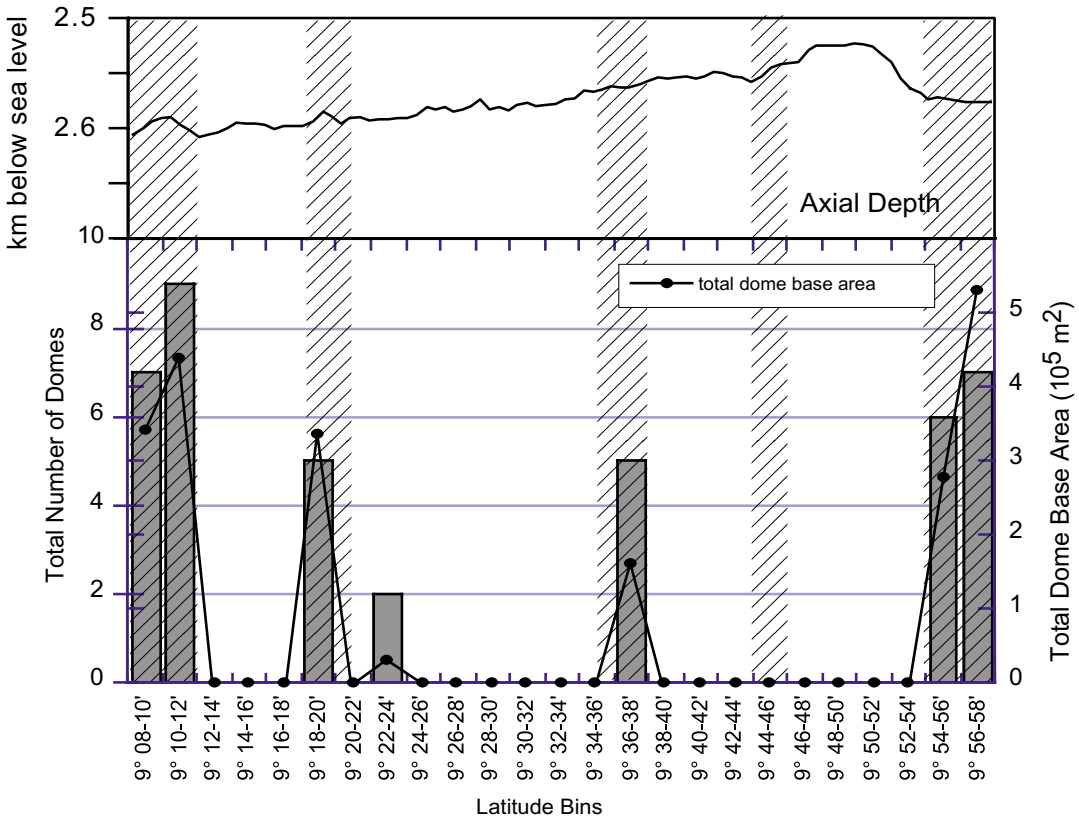

Figure 6

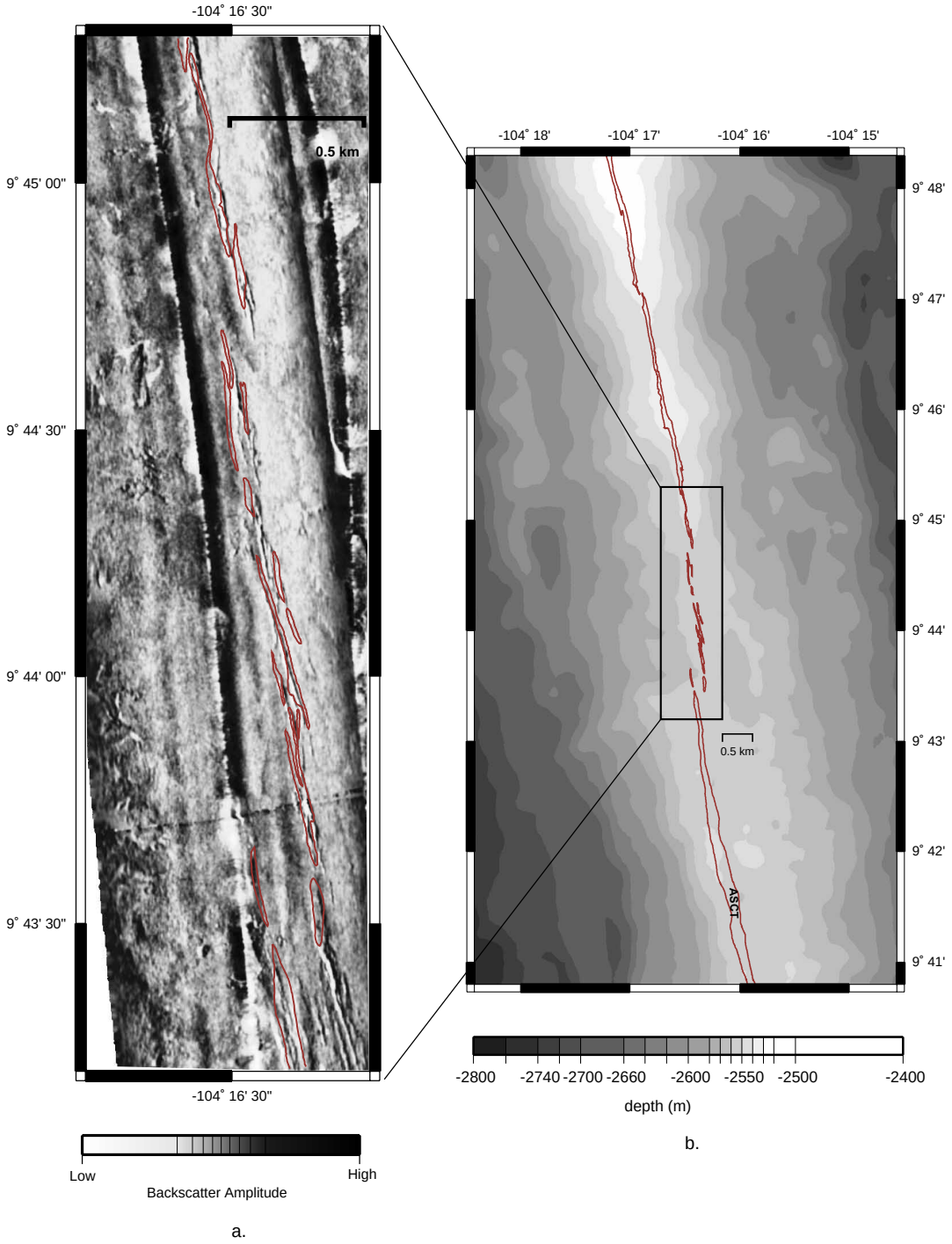
-104˚ 16' 30"
0.5 km
9˚ 45' 00"
9˚ 44' 30"
9˚ 44' 00"
9˚ 43' 30"
-104˚ 16' 30"
Low
High
Backscatter Amplitude
a.
-104˚ 18'
-104˚ 17'
-104˚ 16'
-104˚ 15'
9˚ 48'
9˚ 47'
9˚ 46'
9˚ 45'
9˚ 44'
9˚ 43'
9˚ 42'
9˚ 41'
0.5 km
ASCT
-2800 -2740 -2700 -2660 -2600 -2550 -2500 -2400
depth (m)
b.

Figure 7

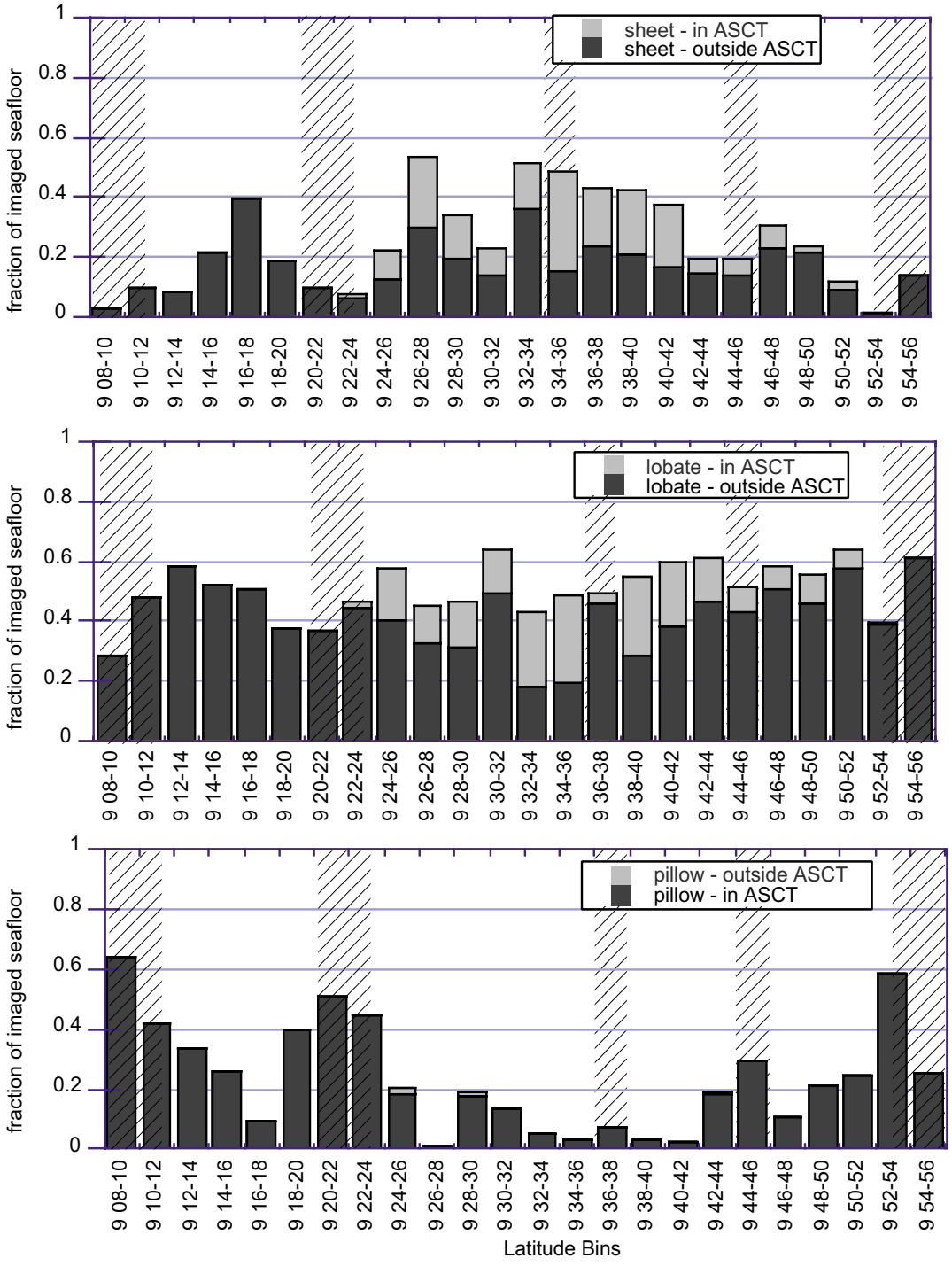
sheet - in ASCT
sheet - outside ASCT
lobate - in ASCT
lobate - outside ASCT
pillow - outside ASCT
pillow - in ASCT
fraction of imaged seafloor
0
0.2
0.4
0.6
0.8
1
9 08-10
9 10-12
9 12-14
9 14-16
9 16-18
9 18-20
9 20-22
9 22-24
9 24-26
9 26-28
9 28-30
9 30-32
9 32-34
9 34-36
9 36-38
9 38-40
9 40-42
9 42-44
9 44-46
9 46-48
9 48-50
9 50-52
9 52-54
9 54-56
Latitude Bins

Figure 8

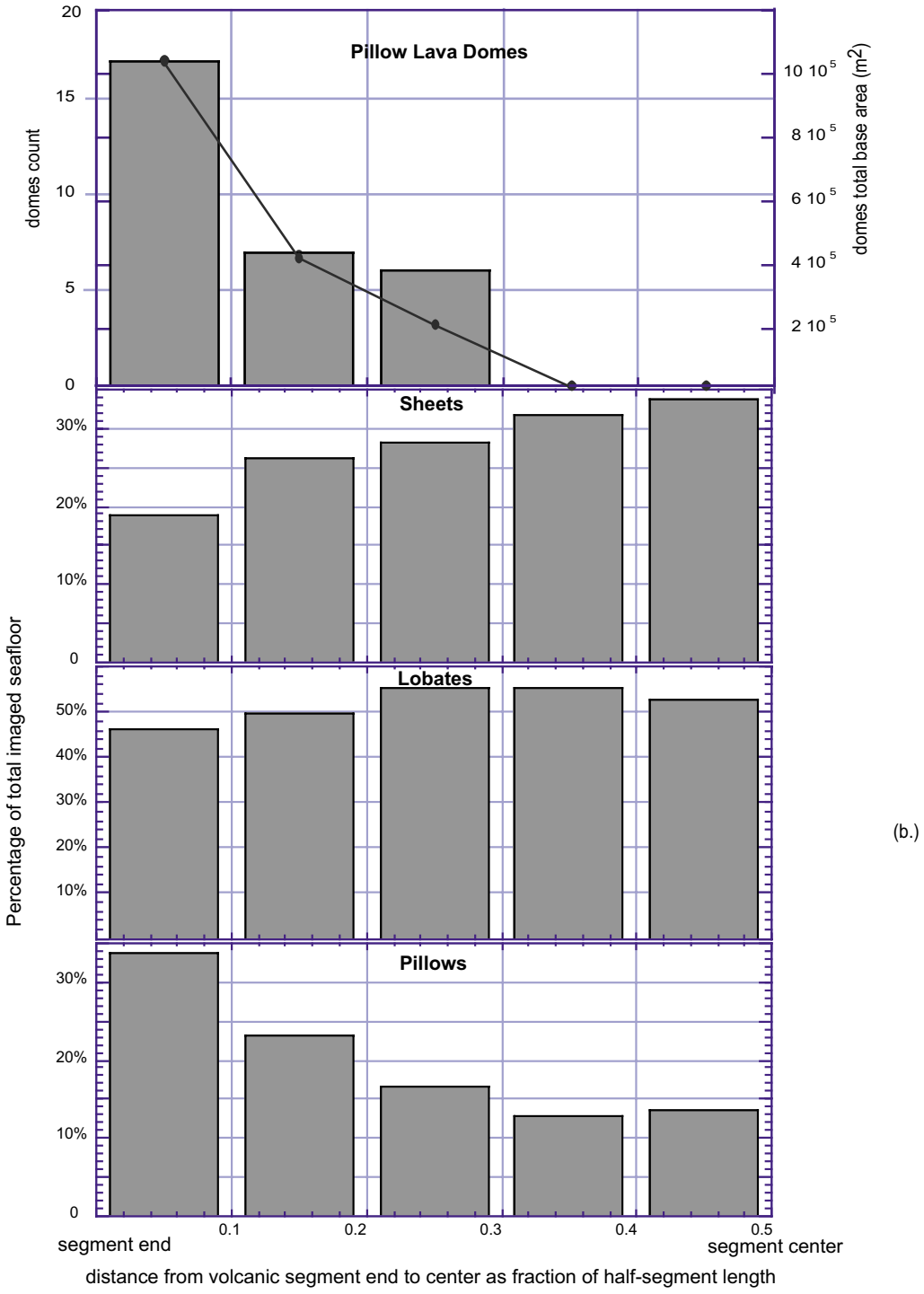
Pillow Lava Domes
domes count
domes total base area (m2)
10 10 5
8 10 5
6 10 5
4 10 5
2 10 5
20
15
10
5
0
(a.)
Sheets
Lobates
Pillows
Percentage of total imaged seafloor
30%
20%
10%
0
50%
40%
30%
20%
10%
0
0.1
0.2
0.3
0.4
0.5
segment end
segment center
distance from volcanic segment end to center as fraction of half-segment length
(b.)

Figure 9

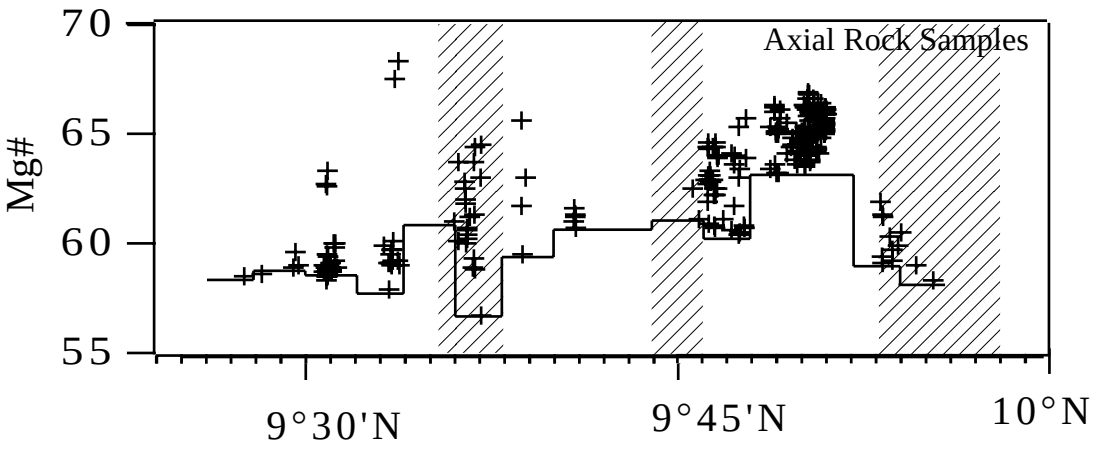

Figure 10

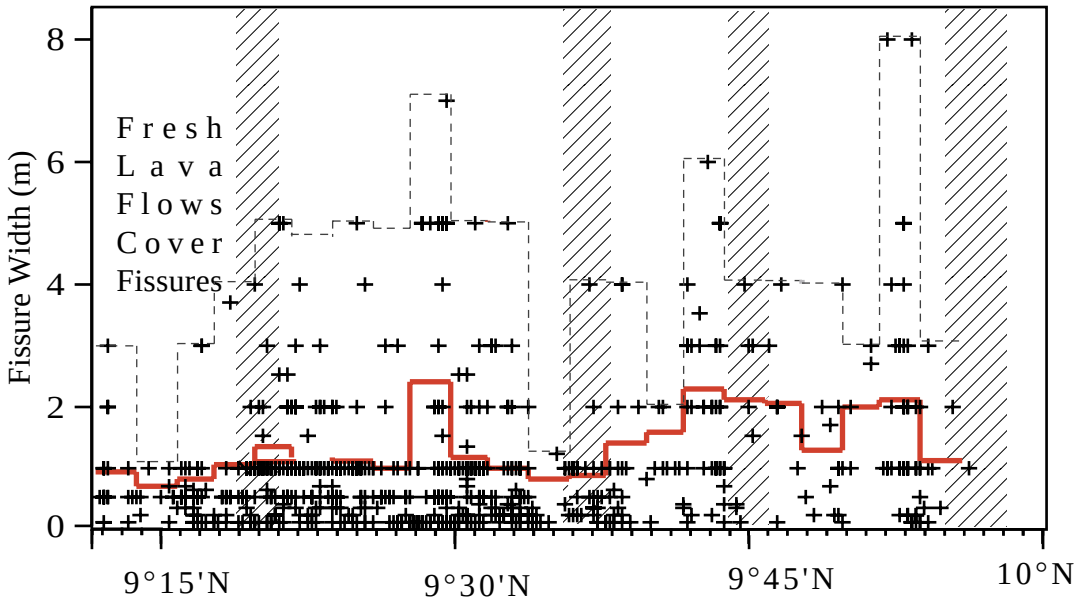

Figure 11

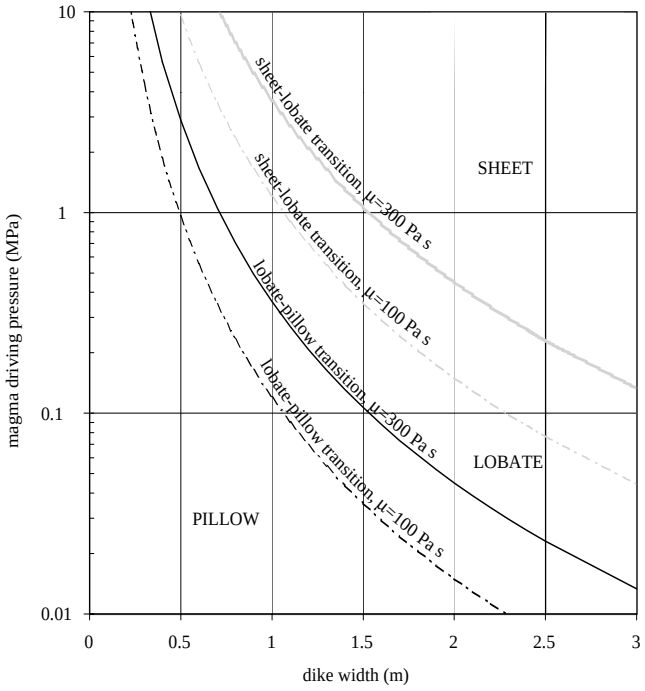
10
1
0.1
0.01
magma driving pressure (MPa)
0
0.5
1
1.5
2
2.5
3
dike width (m)
sheet-lobate transition, μ=300 Pa s
sheet-lobate transition, μ=100 Pa s
lobate-pillow transition, μ=300 Pa s
lobate-pillow transition, μ=100 Pa s
SHEET
LOBATE
PILLOW

Figure 12

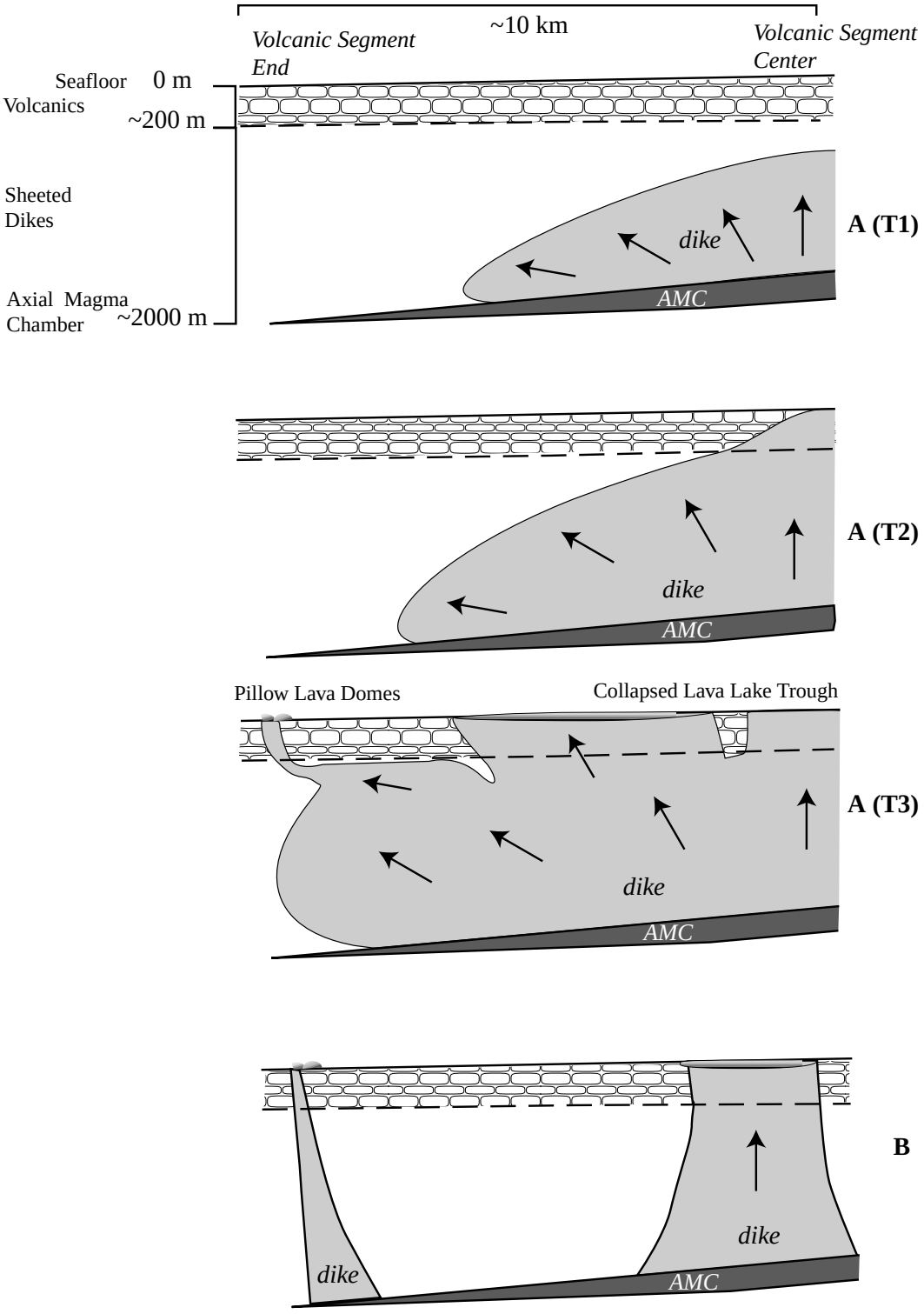
~10 km
Volcanic Segment End
Volcanic Segment Center
Seafloor Volcanics
0 m
~200 m
Sheeted Dikes
Axial Magma Chamber
~2000 m
dike
AMC
A (T1)
dike
AMC
A (T2)
Pillow Lava Domes
Collapsed Lava Lake Trough
dike
AMC
A (T3)
dike
dike
AMC
B

Figure 13